Astronomy & Astrophysics manuscript no. 17123
July 5, 2011

© ESO 2011

arXiv:1107.0661v1 [astro-ph.CO] 4 Jul 2011

Multiwavelength campaign on Mrk 509

VI. HST/COS observations of the far-ultraviolet spectrum ⋆

G. A. Kriss[1,2], N. Arav[3], J.S. Kaastra[4,5], J. Ebrero[4], C. Pinto[4], B. Borguet[3], D. Edmonds[3], E. Costantini[4], K. C. Steenbrugge[6,7], R.G. Detmers[4,5], E. Behar[8], S. Bianchi[9], A. J. Blustin[10], G. Branduardi-Raymont[11], M. Cappi[12], M. Mehdipour[11], P. Petrucci[13], and G. Ponti[14]

[1] Space Telescope Science Institute, 3700 San Martin Drive, Baltimore, MD, 21218, USA e-mail: `gak@stsci.edu`
[2] Department of Physics & Astronomy, The Johns Hopkins University, Baltimore, MD, 21218, USA
[3] Department of Physics, Virginia Tech, Blacksburg, VA 24061, USA
[4] SRON Netherlands Institute for Space Research, Sorbonnelaan 2, 3584 CA Utrecht, The Netherlands
[5] Astronomical Institute, University of Utrecht, Postbus 80000, 3508 TA Utrecht, The Netherlands
[6] Instituto de Astronomía, Universidad Católica del Norte, Avenida Angamos 0610, Casilla 1280, Antofagasta, Chile
[7] Department of Physics, University of Oxford, Keble Road, Oxford OX1 3RH, UK
[8] Department of Physics, Technion, Haifa 32000, Israel
[9] Dipartimento di Fisica, Universita degli Studi Roma Tre, via della Vasca Navale 84, I-00146 Roma, Italy
[10] Institute of Astronomy, University of Cambridge, Madingley Road, Cambridge CB3 0HA, UK
[11] Mullard Space Science Laboratory, University College London, Holmbury St. Mary, Dorking, Surrey, RH5 6NT, UK
[12] INAF-IASF Bologna, Via Gobetti 101, I-40129 Bologna, Italy
[13] UJF-Grenoble 1 / CNRS-INSU, Institut de Planétologie et d'Astrophysique de Grenoble (IPAG) UMR 5274, Grenoble, F-38041, France
[14] School of Physics and Astronomy, University of Southampton, Highfield, Southampton SO17 1BJ, UK

Accepted 26 May 2011

ABSTRACT

We present medium-resolution ($\lambda/\Delta\lambda \sim 20,000$) ultraviolet spectra covering the 1155–1760 Å spectral range of the Seyfert 1 galaxy Mrk 509 obtained using the Cosmic Origins Spectrograph (COS) on the Hubble Space Telescope (HST). Our observations were obtained simultaneously with a Low Energy Transmission Grating Spectrometer observation using the *Chandra* X-ray Observatory, and they are part of a multiwavelength campaign in September through December 2009 which also included observations with *XMM-Newton*, Swift, and INTEGRAL. Our spectra are the highest signal-to-noise observations to date of the intrinsic absorption components seen in numerous prior ultraviolet observations. To take advantage of the high signal-to-noise ratio, we describe special calibrations for wavelength, flat-field and line-spread function corrections that we applied to the COS data. We detect additional complexity in the absorption troughs compared to prior observations made with the Space Telescope Imaging Spectrograph (STIS) on HST. We attribute the UV absorption to a variety of sources in Mrk 509, including an outflow from the active nucleus, the interstellar medium and halo of the host galaxy, and possible infalling clouds or stripped gaseous material from a merger that are illuminated by the ionizing radiation of the active nucleus. Variability between the STIS and COS observation of the most blue-shifted component (#1) allows us to set an upper limit on its distance of < 250 pc. Similarly, variability of component 6 between FUSE observations limits its distance to < 1.5 kpc. The absorption lines in all components only partially cover the emission from the active nucleus with covering fractions that are lower than those seen in the prior STIS observations and are comparable to those seen in spectra from the Far Ultraviolet Spectroscopic Explorer (FUSE). Given the larger apertures of COS and FUSE compared to STIS, we favor scattered light from an extended region near the active nucleus as the explanation for the partial covering. As observed in prior X-ray and UV spectra, the UV absorption has velocities comparable to the X-ray absorption, but the bulk of the ultraviolet absorption is in a lower ionization state with lower total column density than the gas responsible for the X-ray absorption. We conclude that the outflow from the active nucleus is a multiphase wind.

Key words. Galaxies: Active – Galaxies: Individual (Mrk 509) – Galaxies: Quasars: Absorption Lines – Galaxies: Seyfert – Ultraviolet: Galaxies – X-Rays: Galaxies

1. Introduction

Outflows from galaxies powered by an active galactic nucleus (AGN) may play an important role in the chemical enrichment of the intergalactic medium (IGM). The most distant AGN known, quasars at redshifts of 6 or more, have abundances at solar or super-solar levels (Hamann & Ferland 1993, 1999; Pentericci et al. 2002; Barth et al. 2003; Dietrich et al. 2003; Freudling et al. 2003; Juarez et al. 2009). Although the chemical enrichment of the host likely predates the presence of the active nucleus (Simon & Hamann 2010), winds powered by the AGN could return this metal-enriched material to the IGM (Furlanetto & Loeb 2001; Cavaliere et al. 2002; Germain et al.

⋆ Based on observations made with the NASA/ESA Hubble Space Telescope, obtained at the Space Telescope Science Institute, which is operated by the Association of Universities for Research in Astronomy, Inc., under NASA contract NAS 5-26555. These observations are associated with program # 12022.

2009; Hopkins & Elvis 2010; Barai et al. 2011). Their presence and feedback may also have a significant impact on the evolution of their host galaxies (Silk & Rees 1998; Scannapieco & Oh 2004; Granato et al. 2004; Di Matteo et al. 2005; Hopkins et al. 2008; Somerville et al. 2008). While some fraction of these outflows in low-luminosity AGN may not escape their host galaxy, at least as measured in the local universe (Das et al. 2005; Ruiz et al. 2005; Das et al. 2007), the impact of the outflow on lower-density portions of the host interstellar medium (ISM) could provide a significant transport mechanism for the enrichment of the surrounding environment (Hopkins & Elvis 2010). From constraints provided by the X-ray background, such lower luminosity AGN may dominate the population of active galaxies in the early universe (Treister et al. 2009, 2010).

Nearby AGN provide local analogs that can help us to understand the mechanics, energetics, and chemical enrichment patterns that may play a significant role in cosmic evolution at high redshift. More than half of low-redshift AGN exhibit blue-shifted UV or X-ray absorption features indicative of outflowing gas (Crenshaw et al. 2003; Dunn et al. 2007; Cappi et al. 2009; Tombesi et al. 2010). Understanding the geometry and the location of the outflow relative to the active nucleus is a key to making an accurate assessment of the total mass and the kinetic luminosity of the outflow. Distance determinations are particularly difficult. Using density-sensitive absorption lines to establish the gas density, in combination with photoionization models that reproduce the observed relative column densities can provide precise distance estimates. These measures have ranged from tens of parsecs in NGC 3783 (Gabel et al. 2005b) and NGC 4151 (Kraemer et al. 2006, if one uses the correct critical density for C III*), and up to kiloparsec scales in some quasars and AGN (Hamann et al. 2001; Scott et al. 2004; Edmonds et al. 2011). UV and X-ray observations of Mrk 279 (Scott et al. 2004; Arav et al. 2007; Costantini et al. 2007) measured absolute abundances in the outflow of a local AGN for the first time, and they show evidence for enhanced CNO abundances that suggest contributions from massive stars and AGB stellar winds.

To improve upon these prior studies, we have conducted a multiwavelength campaign of coordinated X-ray, UV, and optical observations of the nearby luminous Seyfert 1 galaxy Mrk 509 (z=0.034397; Huchra et al. (1993)). A complete overview of the campaign is given by Kaastra et al. (2011b). Mrk 509 is an ideal object for study due to its high flux, moderate luminosity that rivals that of QSOs (Kopylov et al. 1974), and deep, well structured absorption troughs. The blue-shifted absorption indicative of a nuclear outflow has been known since the earliest UV spectral observations (Wu et al. 1980; York et al. 1984). The outflow is also apparent in the blueshifted [O III] emission detected across the face of Mrk 509 by Phillips et al. (1983). More recently Kriss et al. (2000) and Kraemer et al. (2003) observed Mrk 509 at high spectral resolution in the UV with the Far Ultraviolet Spectroscopic Explorer (FUSE) and the Space Telescope Imaging Spectrograph (STIS) on the Hubble Space Telescope (HST), respectively. The STIS observations were simultaneous with earlier *Chandra* X-ray grating observations (Yaqoob et al. 2003) that also detect blue-shifted X-ray absorption lines. These prior UV observations show the presence of more than seven distinct kinematic components, none of which could be unambiguously associated with the absorption detected in the X-ray, although both the X-ray and UV absorption do overlap in velocity.

Our newer observations using the Cosmic Origins Spectrograph (COS) on HST achieve higher signal-to-noise ratios (S/N) and provide insight into long-term changes in the absorbing gas. Our COS spectra provide a higher-resolution view of the velocity structure in the outflowing gas, and sample lower ionization ionic species than are present in the X-ray spectra. At high spectral resolution and high S/N, we can use velocity-resolved spectral coverage of the N V and C IV doublets to solve for the covering fractions and column densities in the outflowing gas (Arav et al. 2007). Using our COS observations of Lyα together with the archival FUSE observations of the higher-order Lyman lines, we can provide an absolute reference for abundances relative to hydrogen, which cannot be measured directly in the X-ray spectra. These higher S/N spectra combined with the higher S/N X-ray spectra permit a more detailed examination of the links between the UV and the X-ray absorbing gas in the outflow.

This paper describes the COS observations that are part of our multiwavelength campaign on Mrk 509, and presents an initial interpretation of the results. In §2 we describe our COS observations and our data reduction methods, including enhanced calibrations for the COS data and corrections for the line-spread function. In §3 we describe our analysis of the UV spectra and compare them to prior STIS and FUSE observations of Mrk 509. Finally, in §4 we discuss the physical implications of our observations for the geometry and location of the absorbing gas in Mrk 509 and its physical conditions. We end with a summary of our conclusions in §5.

2. Observations and Data Reduction

As part of our extensive coordinated campaign on Mrk 509 (Kaastra et al. 2011b), we observed Mrk 509 using the Far-Ultraviolet Channel and the medium-resolution gratings of the Cosmic Origins Spectrograph (COS) on the Hubble Space Telescope (HST). Descriptions of COS and its on-orbit performance can be found in the COS Instrument Handbook (Dixon et al. 2010). Our two visits on 2009 December 10 and 11 were simultaneous with the *Chandra* observations described by Ebrero et al. (2011). Using gratings G130M and G160M and observing through the Primary Science Aperture (PSA), we covered the far-ultraviolet spectral range from 1155 Å to 1760 Å. The instrument configurations, times of observation, and integration times are summarized in Table 1. For each grating, we used only two tilts to avoid placing gaps in spectral ranges of interest surrounding the strong emission and absorption features in Mrk 509. This resulted in almost complete spectral coverage except for a small gap from 1560–1590 Å. The two tilts and two exposures at each setting resulted in four independent placements of the grid-wire shadows and other instrumental artifacts along the spectrum. This enhanced our ability to flat field these high signal-to-noise ratio data. Exposure times were weighted more heavily in favor of grating G160M since Mrk 509 is fainter across this wavelength range, and the throughput of G160M is lower relative to G130M. This gives more uniform signal-to-noise ratios across the full spectrum. For G130M we obtained a total exposure time of 9470 s; for G160M, the total exposure time was 16452 s.

Our data were processed with the COS calibration pipeline v2.11b at STScI. This version of the pipeline does not correct for flat-field features or the time-dependent sensitivity of COS, and there are still some residual anomalies in the wavelength calibration. To produce the best quality summed data set, we used a customized series of procedures to make these corrections as described in the following sections.

Table 1. COS Observations of Mrk 509

Data Set Name	Grating/Tilt	Date	Start Time (GMT)	Exposure Time (s)
lbdh01010	G130M/1309	2009-12-10	02:48:40	1993
lbdh01020	G130M/1327	2009-12-10	04:07:03	2742
lbdh01030	G160M/1577	2009-12-10	05:42:57	5484
lbdh01040	G160M/1589	2009-12-10	08:54:42	2742
lbdh02010	G130M/1309	2009-12-11	02:46:46	1993
lbdh02020	G130M/1327	2009-12-11	04:05:12	2742
lbdh02030	G160M/1577	2009-12-11	05:41:05	2742
lbdh02040	G160M/1589	2009-12-11	07:16:57	5484

2.1. Flat-Field Corrections

To flat field the data and correct for instrumental artifacts, we used one-dimensional flat-field corrections developed from COS observations of white dwarf standards (Ake et al. 2010). These flat fields correspond to each detector segment (A and B) for each grating (G130M and G160M) we used. The signal-to-noise ratio in these flat fields (in terms of purely Poisson-distributed noise) is comparable to that in our data set. To reduce the impact of the added noise that would result from dividing by these data for our flat-field correction, we first smoothed the flat-fields. It may seem counterintuitive to consider smoothing pixel-to-pixel flats when using them to correct for pattern noise and artifacts, but there are two fundamental reasons why this works. First, real artifacts and pattern noise are never sharper than the intrinsic resolution of the detector, which is approximately six pixels. Second, drifts in the grating select mechanism, which are corrected during an observation using the TAG-FLASH observing mode, effectively smear the pattern noise. Since our observations were longer than any of the individual ones used to develop the one-dimensional flats, the smearing of the pattern noise is greater. Smoothing the flats partially corrects for this smearing. After trying a variety of smoothing widths, we settled on smoothing the flats with a Gaussian profile having a 1-pixel dispersion. To align the flats with the extracted 1D spectra from each exposure, we cross correlated the appropriate smoothed flat with the data, applied an appropriate integer-pixel shift, and then divided it out.

Once the data were flat-field corrected, we aligned the individual exposures by first cross-correlating them with each other and applying the closest integer-pixel shift. While this process produced a tremendous improvement in the data, some residual features remained. We then examined each individual exposure, comparing them with each other and with the flat field used to correct them. Strong features in the flats that did not divide out well were then flagged in the individual exposures so that they could be excluded when we did the final combination. Our final spectrum for each grating is the exposure-weighted combination of the unflagged pixels in each of the individual flat-fielded and aligned exposures. Although our data would support a signal-to-noise ratio of over 100 per pixel in the Poisson limit, we do not do much better than 60:1 per pixel in our final spectrum.

2.2. Wavelength Calibration

While the nominal wavelength calibration of COS over most of the spectral range has errors less than 15 km s^{-1}, this is not adequate for our analysis. We wish to align spectral features (both intrinsic to Mrk 509 and in intervening material) more accurately for comparison in velocity space, and for comparison to prior observations with FUSE and STIS. There can also be residual zero-point shifts in the wavelength scale due to offsets from the aperture center which may not have been fully removed in the target acquisition process. Therefore, we first adjusted the wavelength-scale zero points for our G130M and G160M spectra by cross correlating them with the prior STIS observation of Mrk 509. For G130M, we used the wavelength region from 1245–1290 Å, which is dominated by the intrinsic absorption features from Lyα and N v. For G160M, we used the region from 1590–1615 Å, centered on the intrinsic absorption from C iv. The intrinsic absorption features provide numerous sharp edges that result in a strong, narrow cross-correlation peak that enhances the precision of the alignment. The resulting corrections were < 0.1 Å.

For the next level of correction, we used the numerous interstellar absorption lines in our spectra that spanned the full wavelength range. As the sight line to Mrk 509 is very complex, each interstellar line typically has multiple components. The H I 21-cm emission in this direction (Murphy et al. 1996) has a strong flux-weighted peak at +3.1 km s^{-1} in the local standard of rest (LSR), and a weaker, broader peak at $\sim$ +65 km s^{-1} (LSR). The +3 km s^{-1} feature is present in all detected interstellar lines, and the +65 km s^{-1} one is present in the stronger lines. In addition, there are high-velocity features at −249 and −295 km s^{-1} visible in the strongest lines and in the higher ionization species like C iv. We measured the wavelengths of all these interstellar features. The wavelength differences of our measurements relative to vacuum wavelengths show a systematic, nearly linear trend with wavelength across each detector segment that amount to an offset of 0.06 Å from one end of each segment to the other. We take this as an indication that there is a slight error in the dispersion constant for the COS wavelength calibration. To weight our correction by the strongest features, we used only those corresponding to the +3 and +65 km s^{-1} components and performed a linear fit to the wavelength offsets for each detector segment. We then made a linear correction to the wavelength scale, with pivot points that have zero correction about 1260 Å and 1600 Å so that we keep our zero points aligned with the STIS wavelength scale. After applying this correction, we then find a peak-to-peak variation among the velocity offsets of all the interstellar features of −10 to +8 km s^{-1}, with a dispersion of 4.3 km s^{-1}.

2.3. Flux Calibration

The sensitivity of COS has been slowly declining since its installation (Osten et al. 2010). We have applied the time-dependent sensitivity corrections to our data as given by Osten et al. (2010). These corrections amount to an adjustment of only 2.5% at the short wavelength end of the G130M spectrum, and range up to a correction of 5% at the long-wavelength end of G160M. We estimate an absolute flux accuracy of 5% at wavelengths above 1220 Å, and 10% at shorter wavelengths (Massa et al. 2010). We

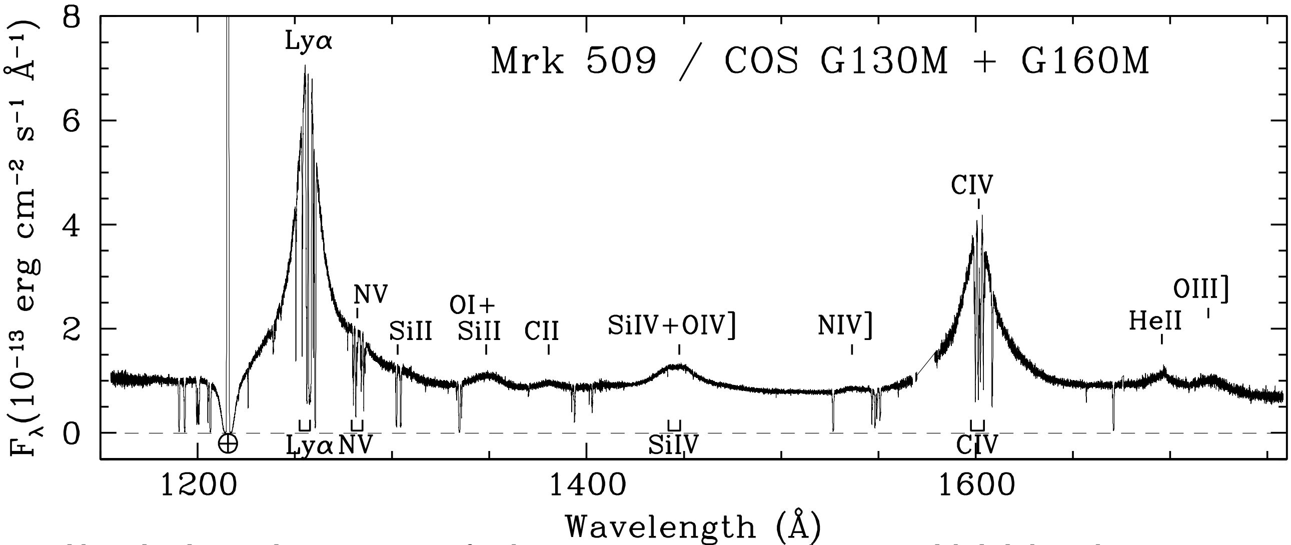

Fig. 1. Calibrated and merged COS spectrum of Mrk 509. Prominent emission features are labeled above the spectrum. Regions of intrinsic absorption are indicated below the spectrum. Geocoronal emission in the center of the galactic Lyα absorption trough is indicated with an Earth symbol.

expect that relative fluxes are more precise. Our repeat observations in our two visits agree to better than 1%, and comparison between the overlapping wavelength ranges of G130M and G160M in our spectra show that they also agree to better than 1%.

As an external comparison, and for cross-calibration purposes with the other elements of our campaign, we compare our spectrum to the Swift UVM2 data point from 2010 Dec 10. These data are in a broad band centered at 2231 Å, with some contamination from broad C iii] emission (Mehdipour et al. 2011). To compare our COS spectrum to this point requires some extrapolation. We take the 1140–8090 Å spectrum assembled by Shang et al. (2005) from FOS and KPNO 2.1-m spectra, and normalize this spectrum to the corrected Swift UVM2 continuum flux at 2231 Å of 5.12×10^{-14} ergs cm^{-2} s^{-1} Å^{-1} (Mehdipour et al. 2011). At wavelengths longer than 1220 Å, our COS spectra agree with the FOS spectrum normalized to the corrected Swift UVM2 flux to better than 4% at all wavelengths. Below 1210 Å, our COS spectrum is brighter by up to 9% above the renormalized FOS spectrum. This could be a true difference in the spectrum, but it could also be an indication of our residual uncertainties in the flux calibration. In the latter case, we conservatively estimate that our absolute flux below 1220 Å is better than 10%.

Figure 1 shows our calibrated and merged COS spectra. We have labeled the prominent emission features in the spectrum as well as the regions containing the intrinsic absorption features. The many galactic interstellar absorption lines in our spectrum are not labeled here. In an on-line appendix available only in the journal version of this paper, Fig. A1 shows full-resolution plots of the COS spectrum of Mrk 509.

2.4. STIS Spectrum

The STIS spectrum is a 7,600 s observation obtained on 2001-04-13 using the echelle E140M grating and the 0.2×0.2 arc sec aperture (Kraemer et al. 2003; Yaqoob et al. 2003, Proposal ID 8877, PI: Yaqoob). The spectrum we use is the one-dimensional extracted echelle spectrum direct from the MAST archive with all up-to-date calibrations applied, including corrections for scattered light in the echelle mode (Valenti et al. 2002) and for the echelle blaze corrections (Aloisi et al. 2007). The STIS spectrum of Mrk 509 has a resolution about twice that of the COS spectra, R=46,000. This spectrum is particularly useful for assessing the true resolution of the COS spectrum, and the validity of deconvolutions that repair the broad wings of the COS line-spread function.

To illustrate the dramatic improvement in the quality of our COS data compared to the prior STIS observation, Figure 2 shows a portion of both spectra in the region centered around the Lyα absorption feature intrinsic to Mrk 509. One sees that Mrk 509 was ~60% brighter during our COS observation. In addition, the higher throughput of COS also improves our resulting signal-to-noise ratio by a factor of ~5. However, one can see that there are still instrumental features that we must correct before doing a detailed analysis of the COS data. Deep, saturated absorption features in the STIS spectrum, especially the interstellar Si ii line at 1260.5 Å, do not have square, black troughs in the COS spectrum. This is due to the broad wings on the line-spread function (LSF) (Ghavamian et al. 2009) that redistribute light from the bright continuum into cores of the absorption lines. To extract the maximum information from our spectrum, we must correct for these broad wings on the LSF.

2.5. Deconvolving the COS Spectrum

The broad wings on the COS LSF are caused by mid-frequency polishing errors on the HST primary & secondary mirrors (Ghavamian et al. 2009). Additional scattering by the HST mirror system and internal to COS makes these wings more extensive than originally thought (Kriss 2011). These errors must be removed in order to obtain accurate measurements of the depths of the absorption lines in the COS spectrum. On scales less than about 50 km s^{-1}, significant light can leak into the absorption line troughs from adjacent continuum regions. As a result, interstellar absorption lines expected to be saturated are not black.

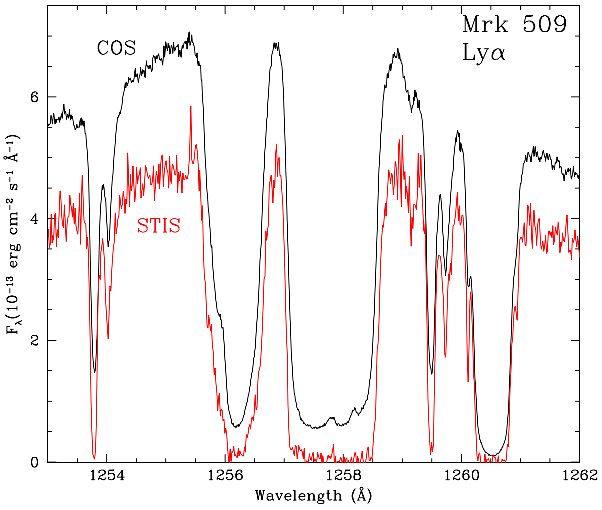

Fig. 2. COS spectrum of Mrk 509 in the Lyα region (black) compared to the STIS spectrum (red).

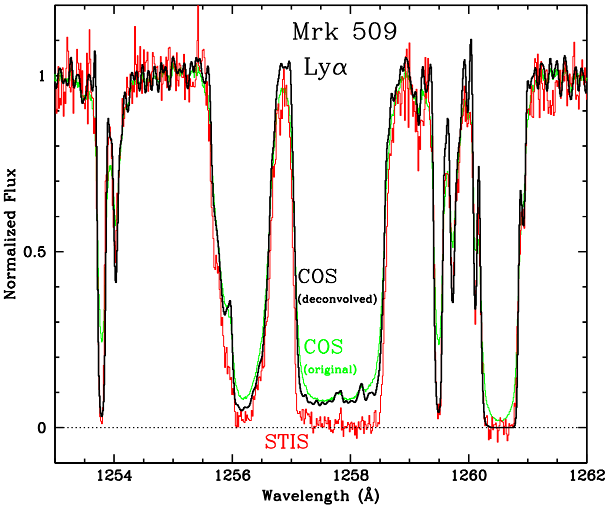

Fig. 3. Comparison of the deconvolved COS spectrum in the spectral region surrounding the Lyα absorption trough (black) to the original COS spectrum (green) and the STIS spectrum (red).

This is quite obvious when one compares the interstellar lines in the COS spectrum in Fig. 2 to the prior spectrum obtained with STIS.

The high signal-to-noise ratio of our data permits us to do a fairly good job of deconvolving the line-spread function from our data. We use the Lucy-Richardson algorithm to deconvolve the data as implemented in the STSDAS routine “lucy” in the analysis.restore package. We deconvolve the spectrum in 50 Å intervals using the updated versions of the wavelength-dependent LSFs from the COS web site at STScI (Kriss 2011). The deconvolution converges well after ∼20 iterations. A good illustration of the success of our deconvolution is provided by direct comparisons to the higher-resolution STIS spectrum of Mrk 509. Figure 3 shows the normalized version of the original COS spectrum in the Lyα region, the deconvolved spectrum, and the STIS spectrum, all plotted together. The deconvolution deepens the narrow interstellar absorption features so that they match the higher-resolution STIS spectra well. Broader, saturated interstellar lines like Si ii λ1260.5 have square, black bottoms. Overall, the deconvolved, high S/N COS spectrum looks like an excellent fit to the STIS spectrum. One disadvantage to the deconvolution, however, is that it amplifies noise in the continuum. This can obscure weak absorption features. Therefore, in our analysis we will adopt the approach of using the original spectrum to identify significant features, but use the deconvolved spectrum to make accurate measurements of the strength of known features so that the effects of the LSF are fully corrected.

2.6. FUSE Spectra

FUSE (Moos et al. 2000) observed Mrk 509 on two different occasions during the mission. The first FUSE spectrum, obtained in two closely spaced observations on 1999-11-02 (19,355 s) and 1999-11-06 (32,457 s), were analyzed and discussed by Kriss et al. (2000). The second FUSE visit (Observation ID P1080601) was a 62,100 s observation obtained on 2000-09-05. We retrieved these data from the MAST archive and reprocessed them with a customized version of the FUSE pipeline, using only the night portions of the observation in order to minimize airglow and background. Our version of the processing also lowers the background noise by screening out more of the lowest pulse height channels. We cross correlate the overlapping wavelength sections of each channel to align the wavelength scales, and renormalize all the fluxes to match channel LiF1A, which was aligned with the fine guidance sensor for both observations. We correct for the “worm” in segment LiF2A by taking a ratio to the matching portion of the spectrum in LiF1B, fitting a spline, and applying that correction to LiF2A. We then combine all channels in overlapping wavelength regions weighted by the S/N of the individual pixels. Although Mrk 509 was fainter in 2000 compared to the first observation, channel alignment was better, and the overall S/N is higher. Mrk 509 was fainter in both FUSE observations than in our current COS observation by 34% to 55%.

3. Data Analysis

3.1. Continuum and Emission Lines

Our first step in analyzing the absorption features in Mrk 509 is to fit the line and continuum emission. We use the specfit task in the contrib package of IRAF for our fits (Kriss 1994). For the continuum, we use a reddened power law ($F_\lambda = F_{1000}\ (\lambda/1000\text{Å})^{-\alpha}$) with extinction of E(B-V) = 0.057 (as obtained from NED via the prescription of Schlegel et al. 1998) and variation with wavelength as specified by Cardelli et al. (1989) with a ratio of selective to total extinction of $R_V = 3.1$. Our best-fit power law has $F_\lambda = 2.48\times10^{-13}\ (\lambda/1000\text{Å})^{-1.74}$ ergs cm^{-2} s^{-1} Å^{-1}. A summary of the power law parameters and observed continuum fluxes at 1175 Å for the COS observation and the prior STIS and FUSE observations is given in Table 2.

For the strongest emission lines, our model requires four Gaussian components to give a good fit. For O vi, Lyα, and C iv, we use a broad base, two moderately broad components that comprise most of the line profile, and a narrow-line component of full-width half-maximum (FWHM) of 300 km s^{-1} fixed to match the width of the narrow [O iii] emission in the visible spectrum (Phillips et al. 1983). For the O vi and C iv doublets,

Table 2. Continuum Fits to Observations of Mrk 509

Observatory	Date	F_{1000} (10^{-13} ergs cm^{-2} s^{-1} Å^{-1})	α	F(1175 Å) (10^{-13} ergs cm^{-2} s^{-1} Å^{-1})
FUSE	1999-11-06	1.58	0.41	0.607
FUSE	2000-09-05	0.88	1.16	0.416
HST/STIS	2001-04-13	1.44	1.74	0.538
HST/COS	2009-12-10	2.48	1.74	0.918

we include a component for each line of the doublet with the relative wavelengths fixed at the ratio of the laboratory values, and an optically thin, 2:1 ratio for the blue to the red flux component of the doublet. Weaker lines in the spectrum (e.g., C III, N V, Si IV) require only a moderately broad component. The only other visible narrow line in the far-UV spectral range is a He II λ1640 line. The panels in Fig. 4 show the full emission model overplotted on the COS spectrum of Mrk 509 and the individual emission components for the regions surrounding the Lyα, N V, and C IV emission lines. Tables 3, 4, 5, and 6 give the best fitting parameters for the fitted emission lines in the COS, STIS, and FUSE spectra. We note that the narrow-line components are weak, and they are poorly constrained. They do improve the fit, but since they have such a small contribution to the unabsorbed spectrum, they ultimately have little impact on the properties derived for the absorption lines.

3.2. Foreground absorption features

Given our description of the emission lines and continuum in our spectrum of Mrk 509, we now identify and fit all significant absorption features in the observed spectrum. Most of these features are foreground absorption due to our own interstellar medium, and they will be discussed in detail by Pinto (in preps.). We fit the galactic and intergalactic absorption features using a Gaussian profile in optical depth. Many of the strongest interstellar lines are blends of features at several different velocities. Up to seven individual components are detected in some ISM lines. In cases where we cannot definitively separate these components, we fix their relative velocities at the mean of the velocities observed in cleanly resolved components of other interstellar lines. Our measured velocities and equivalent widths for the identified features are given in Table 7. The tabulated error bars are purely statistical. For the velocities, at a resolution of 15 km s^{-1} and S/N > 50, the statistical errors are expected to be < 1 km s^{-1}. In such cases, we have rounded the values up to 1.

We also find three foreground absorption features that we identify as Lyα absorption in the intergalactic medium as shown in Table 8. One of these features was previously identified by Penton et al. (2000). The second feature at 1221.08 Å is similar to this, but much weaker. The third feature at 1239.03 Å is badly blended with foreground galactic N V λ1238. Given the observed equivalent width of the red component of N V λ1242, this blend is too strong to be simply foreground N V absorption. We attribute the excess (and the slight velocity offset) to an intergalactic Lyα absorber. We observe no other absorption lines in our spectrum associated with these foreground intergalactic systems.

3.3. The Intrinsic Absorption Features

The COS spectrum of Mrk 509 shows a wealth of detail in the intrinsic absorption features. The seven major components originally identified by Kriss et al. (2000) in the FUSE spectrum were expanded to eight by Kraemer et al. (2003) based on their STIS spectrum. Our COS spectrum shows additional subtle inflections indicating that the absorption troughs are a quite complex blend of perhaps even more components than we can readily resolve. Figure 5 shows the intrinsic absorption features detected in our COS spectrum as a function of velocity with the components labeled. For reference, we also include the O VI, Lyβ and Lyγ regions of the spectrum from the FUSE observation of Mrk 509

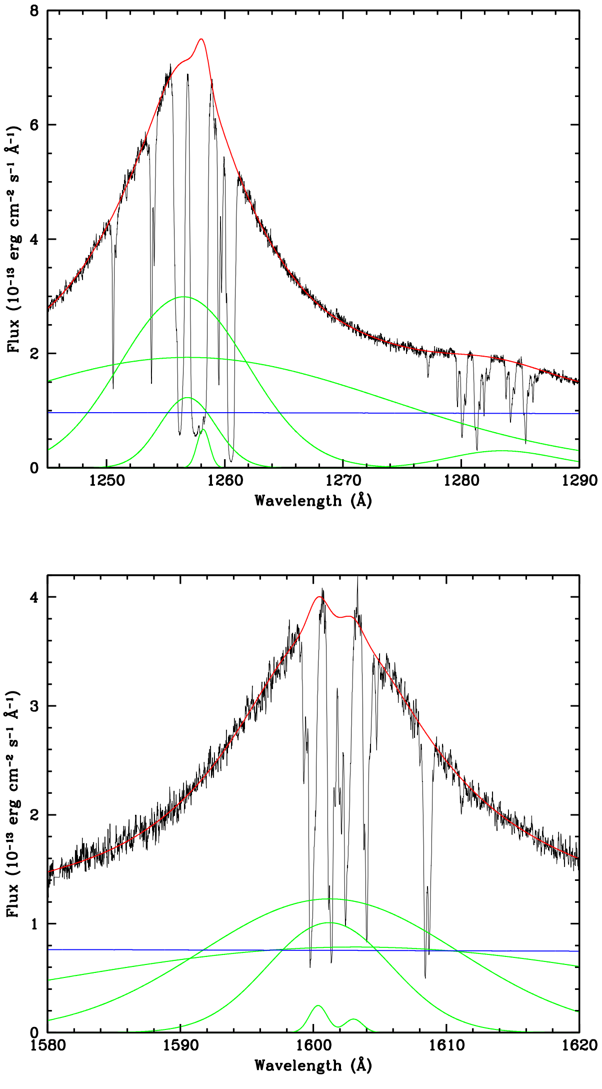

Fig. 4. Fit to the broad lines and continuum of Mrk 509 (red line) is plotted on the observed spectrum (black). Green lines show the individual emission-line components in the fit. The blue line is the continuum. The first panel shows the Lyα and N V region. The second panel shows the C IV region.

Table 7. Interstellar Absorption Features in the COS Spectrum of Mrk 509

Table 7. Interstellar Absorption Features in the COS Spectrum of Mrk 509 (cont.)

Feature	λ_0 (Å)	EW (mÅ)	$V_{\rm LSR}$ (km s^{-1})
C I	1157.91	15 ± 3	−9 ± 1
S III	1190.21	150 ± 18	+2 ± 1
Si II	1190.42	75 ± 7	−48 ± 2
Si II	1190.42	306 ± 13	+7 ± 1
Si II	1190.42	360 ± 34	+65 ± 1
Si II	1190.42	11 ± 2	+143 ± 1
C I	1192.22	10 ± 2	−6 ± 1
Si II	1193.29	56 ± 4	−52 ± 1
Si II	1193.29	329 ± 18	+11 ± 1
Si II	1193.29	345 ± 28	+72 ± 1
Si II	1193.29	12 ± 2	+132 ± 1
Mn II	1197.18	24 ± 3	+5 ± 1
Mn II	1199.39	45 ± 6	+3 ± 1
Mn II	1201.12	14 ± 2	+4 ± 1
N I	1199.55	193 ± 5	+9 ± 1
N I	1199.55	171 ± 4	+74 ± 1
N I	1200.22	173 ± 5	+8 ± 1
N I	1200.22	149 ± 3	+70 ± 1
N I	1200.71	175 ± 5	+6 ± 1
N I	1200.71	115 ± 3	+69 ± 1
Si III	1206.50	202 ± 4	−289 ± 1
Si III	1206.50	59 ± 3	−227 ± 1
Si III	1206.50	11 ± 1	−63 ± 1
Si III	1206.50	417 ± 37	+6 ± 1
Si III	1206.50	477 ± 84	+66 ± 1
Si III	1206.50	26 ± 2	+140 ± 1
N V	1238.82	11 ± 2	−292 ± 1
N V	1238.82	7 ± 2	−236 ± 1
N V	1238.82	37 ± 2	+11 ± 1
N V	1238.82	10 ± 2	+69 ± 1
N V	1242.80	6 ± 2	−294 ± 1
N V	1242.80	4 ± 2	−238 ± 1
N V	1242.80	19 ± 2	+10 ± 1
N V	1242.80	5 ± 2	+68 ± 1
Mg II	1239.93	27 ± 2	+10 ± 1
Mg II	1240.39	16 ± 2	+8 ± 1
S II	1250.58	117 ± 3	+4 ± 1
S II	1250.58	34 ± 2	+60 ± 1
S II	1253.81	138 ± 3	+8 ± 1
S II	1253.81	72 ± 1	+65 ± 1
S II	1259.52	151 ± 2	+4 ± 1
S II	1259.52	85 ± 1	+64 ± 1
S II	1259.52	153 ± 1	+4 ± 1
S II	1259.52	86 ± 14	+64 ± 1
Si II	1260.42	14 ± 2	−291 ± 1
Si II	1260.42	6 ± 3	−96 ± 1
Si II	1260.42	51 ± 6	−61 ± 1
Si II	1260.42	442 ± 15	+11 ± 1
Si II	1260.42	341 ± 11	+75 ± 1
Si II	1260.42	31 ± 4	+134 ± 1
C I	1277.25	51 ± 32	+5 ± 1
P II	1301.87	41 ± 3	+3 ± 1
O I	1302.17	16 ± 6	−292 ± 1
O I	1302.17	6 ± 6	−97 ± 1
O I	1302.17	2 ± 6	−64 ± 1
O I	1302.17	307 ± 9	+7 ± 1
O I	1302.17	277 ± 21	+74 ± 1
O I	1302.17	6 ± 5	+131 ± 1
Si II	1304.37	16 ± 6	−290 ± 1
Si II	1304.37	6 ± 6	−95 ± 1
Si II	1304.37	8 ± 6	−39 ± 13
Si II	1304.37	284 ± 11	+9 ± 1
Si II	1304.37	251 ± 10	+66 ± 1
Si II	1304.37	15 ± 6	+133 ± 1
C I	1328.83	27 ± 4	−1 ± 2
C II	1334.53	76 ± 4	−293 ± 1
C II	1334.53	23 ± 4	−223 ± 1
C II	1334.53	65 ± 4	−59 ± 1
C II	1334.53	496 ± 37	+11 ± 1
C II*	1335.50	444 ± 21	−144 ± 1
C II*	1335.50	150 ± 4	+49 ± 1
C II*	1335.50	105 ± 4	+105 ± 1
Ni II	1317.22	33 ± 8	+3 ± 3
Ni II	1317.22	16 ± 3	+64 ± 1
Ni II	1370.13	41 ± 3	+4 ± 1
Si IV	1393.76	95 ± 4	−298 ± 1
Si IV	1393.76	16 ± 3	−246 ± 1
Si IV	1393.76	19 ± 3	−63 ± 1
Si IV	1393.76	227 ± 14	+8 ± 2
Si IV	1393.76	165 ± 18	+64 ± 3
Si IV	1393.76	7 ± 5	+131 ± 1
Si IV	1402.77	53 ± 3	−297 ± 1
Si IV	1402.77	11 ± 3	−275 ± 3
Si IV	1402.77	7 ± 3	−64 ± 1
Si IV	1402.77	144 ± 7	+9 ± 1
Si IV	1402.77	103 ± 8	+65 ± 2
Si IV	1402.77	2 ± 1	+131 ± 1
Ni II	1454.84	48 ± 5	−6 ± 1
Si IV[a]	1393.76	89 ± 4	−298 ± 1
Si IV	1393.76	14 ± 3	−252 ± 3
Si IV	1393.76	19 ± 3	−67 ± 1
Si IV	1393.76	223 ± 8	+4 ± 1
Si IV	1393.76	160 ± 8	+60 ± 1
Si IV	1393.76	20 ± 4	+126 ± 1
Si IV	1402.77	65 ± 2	−297 ± 1
Si IV	1402.77	14 ± 2	−250 ± 3
Si IV	1402.77	7 ± 2	−62 ± 1
Si IV	1402.77	157 ± 7	+9 ± 1
Si IV	1402.77	116 ± 8	+69 ± 1
Si IV	1402.77	2 ± 2	+131 ± 1
Ni II	1454.84	24 ± 2	−2 ± 2
Ni II	1454.84	11 ± 2	+56 ± 1
Si II	1526.71	25 ± 2	−73 ± 1
Si II	1526.71	408 ± 11	+0 ± 1
Si II	1526.71	340 ± 11	+59 ± 1
C IV	1548.19	245 ± 5	−298 ± 1
C IV	1548.19	78 ± 5	−245 ± 1
C IV	1548.19	19 ± 3	−125 ± 3
C IV	1548.19	22 ± 4	−63 ± 1
C IV	1548.19	336 ± 8	+8 ± 1
C IV	1548.19	293 ± 9	+66 ± 1
C IV	1548.19	18 ± 4	+130 ± 1
C IV	1550.77	170 ± 4	−298 ± 1
C IV	1550.77	52 ± 4	−248 ± 1
C IV	1550.77	1 ± 14	−269 ± 11
C IV	1550.77	10 ± 4	−64 ± 1
C IV	1550.77	251 ± 7	+5 ± 1
C IV	1550.77	178 ± 7	+65 ± 1
C IV	1550.77	11 ± 4	+129 ± 1
C I	1560.31	45 ± 4	−2 ± 1
Fe II	1608.45	22 ± 2	−73 ± 1
Fe II	1608.45	217 ± 5	+2 ± 1
Fe II	1608.45	204 ± 5	+59 ± 1
Fe II	1608.45	19 ± 3	+91 ± 1
Fe II	1611.20	36 ± 4	+2 ± 2
C I	1656.93	72 ± 5	−3 ± 1
C I	1656.93	15 ± 3	+59 ± 1
Al II	1670.79	33 ± 3	−64 ± 8
Al II	1670.79	420 ± 30	+3 ± 1
Al II	1670.79	379 ± 28	+56 ± 2
Al II	1670.79	23 ± 5	+121 ± 4
Ni II	1709.60	63 ± 12	+11 ± 4
Ni II	1709.60	28 ± 6	+69 ± 4
Ni II	1741.55	50 ± 10	+8 ± 6
Ni II	1741.55	20 ± 9	+66 ± 6
Ni II	1751.91	36 ± 13	+3 ± 5
Ni II	1751.91	17 ± 10	+61 ± 5

[a] The prior entries for Si IV $\lambda\lambda$1393,1402 and Ni II λ1454 were for features in the G130M spectrum. These subsequent entries are for features detected in the G160M spectrum.

Table 8. Intergalactic Absorption Features in the COS Spectrum of Mrk 509

Feature	λ_0 (Å)	EW (mÅ)	$v_\odot$ (km s^{-1})
H I	1215.67	31 ± 3	+1345 ± 2
H I	1215.67	200 ± 4	+2561 ± 1
H I	1215.67	72 ± 4	+5772 ± 2

obtained in 2000. The numbering scheme follows that originated by Kriss et al. (2000), but includes the additional component 4′ added by Kraemer et al. (2003). However, instead of continuing to designate additional components with a "prime", we use designations of "a" or "b" for the additional features, with the convention that an "a" subcomponent is blueshifted from the main feature, and a "b" subcomponent is redshifted. Component 4′ in Kraemer et al. (2003) becomes 4a here.

To fit these features with a simple Gaussian decomposition of the profiles as done by Kriss et al. (2000) clearly has limitations built in by the choice of the number and placement of components. Given the complexity of the absorption troughs, a more model-independent approach is preferred. Several previous studies of AGN outflows have used absorption-line doublets to measure the optical depth and covering fraction in discrete, velocity resolved bins (e.g., Hamann et al. 1997; Barlow & Sargent 1997; Arav et al. 1999; Ganguly et al. 1999; NGC 5548: Arav et al. 2002; NGC 3783: Gabel et al. 2003; Mrk 279: Scott et al. 2004; Gabel et al. 2005a). We will apply this method to our spectrum of Mrk 509 in a subsequent publication (Arav, in preps.). In this paper, however, we obtain a preliminary assessment of the column densities and covering fractions of the intrinsic absorption components by fitting the features with Gaussian profiles in optical depth. This enables a more straightforward comparison of our current results to the prior FUSE and STIS observations. Our model also allows for partial covering by each component, as well as a scattered light component that is a wavelength-independent fraction of the underlying emission components. We note that in the case of a single absorbing region with a single partial covering fraction (denoted f_c) that this is observationally indistinguishable from having a scattered light component at a level of $(1 - f_c)$. However, in the case where there is more than one absorbing component that overlaps in velocity with another absorbing component, there is a significant difference. Assuming that the absorbers are statistically independent, in the region of velocity/wavelength space that they overlap, the transmission of light from the source will be less than for either component individually, being the product $(1 - f_{c1})(1 - f_{c2})$. This produces extra dips in the modeled spectrum in the regions of overlap as illustrated in Fig. 6. This is not a qualitatively accurate representation of the profiles of the absorption troughs in our spectrum, which tend to show more smoothly varying profiles. Characterizing the residual light at the bottoms of our absorption troughs with a scattered component that is independent of wavelength provides a better match to the absorption profiles that we observe. For the N v, Si iv, and C iv doublets, we link the relative wavelengths at the ratio of their vacuum wavelengths, and we link the relative optical depths of the red and blue components at a value of 0.5. Since the Lyα absorption appears to be heavily saturated, as noted previously by Kraemer et al. (2003), we fix the covering fraction for each of the Lyα components at the average of the value determined for the corresponding components in the C iv and N v profiles.

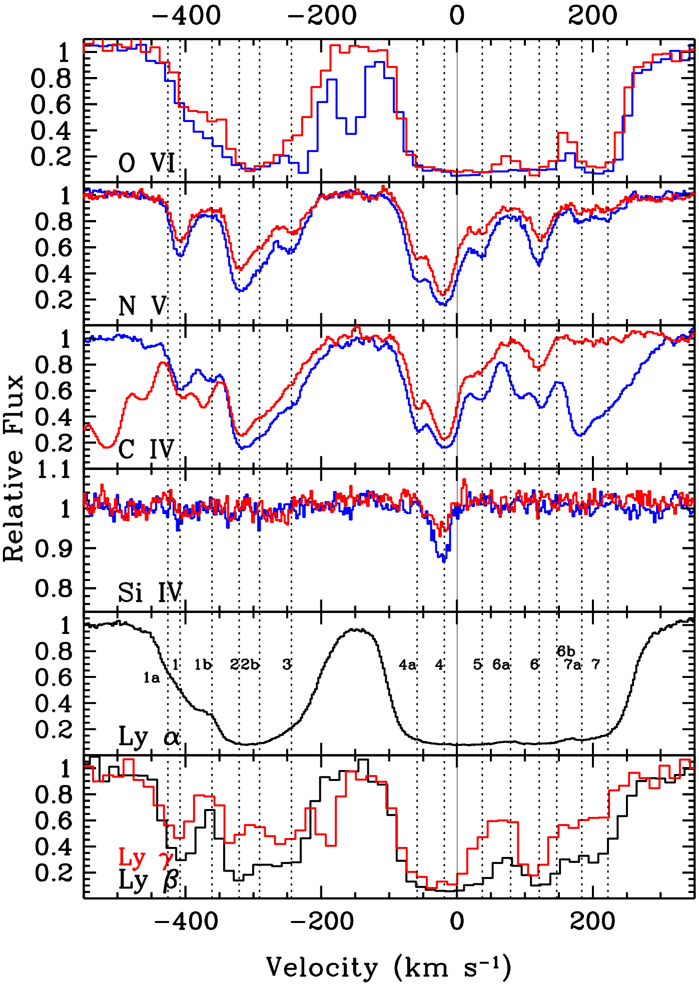

Fig. 5. Intrinsic absorption features in the COS and FUSE spectra of Mrk 509. Normalized relative fluxes are plotted as a function of velocity relative to the systemic redshift of $z = 0.034397$. The top panel shows the O vi doublet from the FUSE observation in 2000 September with the red side of the doublet as a red line and the blue side of the doublet as a blue line. The middle four panels show the N v, C iv, Si iv and Lyα absorption troughs from our COS observation. The bottom panel shows the Lyγ (red) and Lyβ (black) absorption troughs from the FUSE observation. Dotted vertical lines indicate the velocities of identified absorption components. The thin black vertical line shows v = 0.

Our best-fit results are given in Table 9. Note that for Si iv, as in Kraemer et al. (2003), we detect only component 4. Also, as in Kraemer et al. (2003), no lower ionization lines (e.g., Si iii λ1206, Si ii λ1260, or C ii λ1335) are detected. As we noted in §3.1, the narrow emission-line components in our emission model have little impact on the measured properties of the absorption lines. Even if we eliminate the narrow-line emission from our fits, the measured columns densities change by < 1%.

Using the additional components that we have identified in our COS spectra, we have re-analyzed the archival FUSE and STIS spectra of Mrk 509 in order to make a direct comparison among the spectra. While Kriss et al. (2000) have done this for the first FUSE observation, similar measurements for the second observation are useful since they illustrate how the absorbers may change in response to changes in the continuum strength.

Our results from fitting the STIS spectrum are given in Table 10. The column densities for the individual components

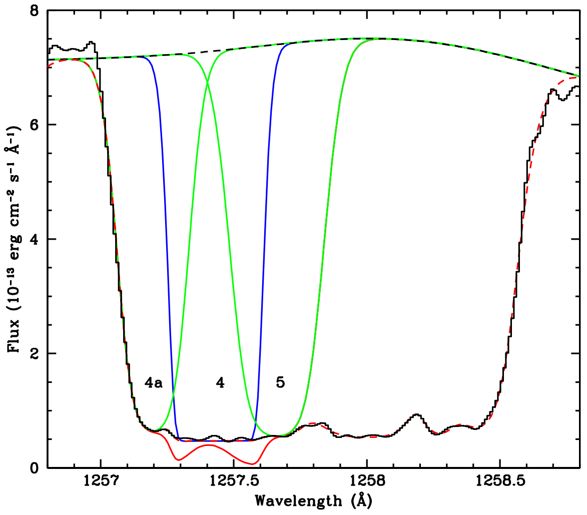

Fig. 6. Fit to a portion of the Lyα absorption trough in the COS spectrum of Mrk 509. The data are shown by the solid black histogram. The red dashed line shows the best fit model using the scattered-light/single partial covering fraction described above for $f_c = 0.064$. The black dashed line shows the emission model for this region. The absorption in this model due to components 4a (shown in green), 4 (shown in blue) and 5 (shown in green) are plotted individually. The solid red line shows the resulting model if these absorbing components each have independent partial covering factors $f_{c,4a} = f_{c,4} = f_{c,5} = 0.064$. The dips in the region of overlap between each component are prominent at wavelengths of ~ 1257.3 Å and 1257.6 Å.

agree well (and within the errors) with those measured by Kraemer et al. (2003) except for the blended components comprising features 2 and 3, and 6 and 7. The apportionment among the various subcomponents accounts for these differences in our fit. We also find a higher column density in the strongest feature, number 4, largely because our width for that component is narrower than that measured by Kraemer et al. (2003).

Results from fits to Lyβ, Lyγ and O vi in the 1999 FUSE spectrum are in Table 11, and results for the 2000 FUSE observation are in Table 12. Since the Lyα absorption trough in Mrk 509 is heavily saturated, the higher-order Lyman lines with good S/N in the FUSE spectrum are particularly useful in deriving reliable column densities and covering factors for H i. However, given potential variability, these values must be used with caution when combined with the data from our COS observations.

In carrying out our fits we found that the well defined features in N v and C iv in the COS spectrum did not always match well with the absorption profiles in Lyα and in O vi. One can see this in Fig. 5, where the Lyα and O vi profiles vary more smoothly. For our best-fit results in Tables 9–12, one can see that some components, such as 1a, are significant only in Lyα, while others, such as 1b, are strongest in O vi. There are also small velocity shifts for other components when comparing N v and C iv to Lyα and O vi. This illustrates the limitations of our Gaussian decomposition, and in §4.2 of the Discussion we address the probable presence of multiple phases of gas at each velocity in the intrinsic absorption troughs.

3.4. Comparison among the COS, STIS and FUSE Spectra

As one can see from the fits to the continua of each of the observations, we have sampled the emission from Mrk 509 over a range of about a factor of two in overall luminosity. The FUSE observation in September 2000 represents the faintest state (0.42×10^{-13} ergs cm^{-2} s^{-1} Å^{-1} at 1175 Å), and the COS observation reported here is the brightest (0.92×10^{-13} ergs cm^{-2} s^{-1} Å^{-1}).

Our COS spectrum of Mrk 509 captures the active nucleus in a significantly brighter state compared to STIS. Overall, the continuum is ~80% brighter. Despite the difference in brightness, the continuum shape does not noticeably change between the STIS and the COS observation. The broad emission lines are also brighter, but not by as much—only 37%. Despite the difference in the continuum level, there are only subtle differences in the absorption-line troughs. The much higher S/N in our COS spectrum reveals some interesting differences from the original STIS spectrum. We show this by comparing the deconvolved COS absorption-line profiles to the STIS profiles in Fig. 7. The biggest differences are in the Lyα absorption profile. Significantly less absorption is present in the most-blue-shifted portions of the trough (essentially components 1–1b). The most striking difference, however, is the extra light that seems to fill the bottom of the Lyα absorption troughs in the COS spectrum, even in the deconvolved version. Comparable differences in the N v and C iv troughs are not readily visible in Fig. 7, so we have carefully examined the COS data to rule out any instrumental effects that might be causing this.

First, we can rule out instrumental scattered light, or residual effects of the line spread function. Since different grating tilts illuminate the detector slightly differently, we compared the separate spectra from each grating tilt and each visit. The extra light in the Lyα trough is visible at both grating tilts, 1309 and 1327, in both visits of our observations. One can readily see in the deconvolved COS spectrum in Fig. 3 that the saturated galactic Si ii λ1260 absorption line is fully corrected to a black trough that is a good match to the STIS spectrum. The much deeper and wider absorption trough at galactic Lyα at 1216 Å is also black, even in the spectrum that has not been deconvolved if one looks at regions that are more than a resolution element removed from the geocoronal Lyα line at the center of the trough. (The peak of the geocoronal Lyα emission is far brighter than the peak of Lyα in Mrk 509, yet the flux drops quickly by over two orders of magnitude from the peak down to the trough of the galactic Lyα absorption.)

Another possibility is that extended emission in Mrk 509, in particular, extended narrow Lyα emission might be filling in the absorption trough. The STIS observation used the 0.2×0.2 arc sec aperture, while the COS entrance aperture is 2.5″ in diameter. Extended emission that is excluded by the STIS aperture could be entering the COS aperture. We examined the 2D spectra, both visually and as summed projections showing the spatial profile, and there is no difference in the spatial extent of the light in the Lyα troughs compared to the continuum. The cross-dispersion profile of the continuum spectrum also shows the nominal width and shape of a point source in the COS aperture. In contrast, the spatial extent of the geocoronal Lyα emission, which fills the aperture, is quite obvious. Of course it is quite bright, but even scaled down it is easily seen to be extended. We conclude that there is no evidence for extended line emission visible in the COS aperture.

Looking closely at the STIS spectrum, one sees that the Lyα absorption is not black at all portions of the trough. In fact,

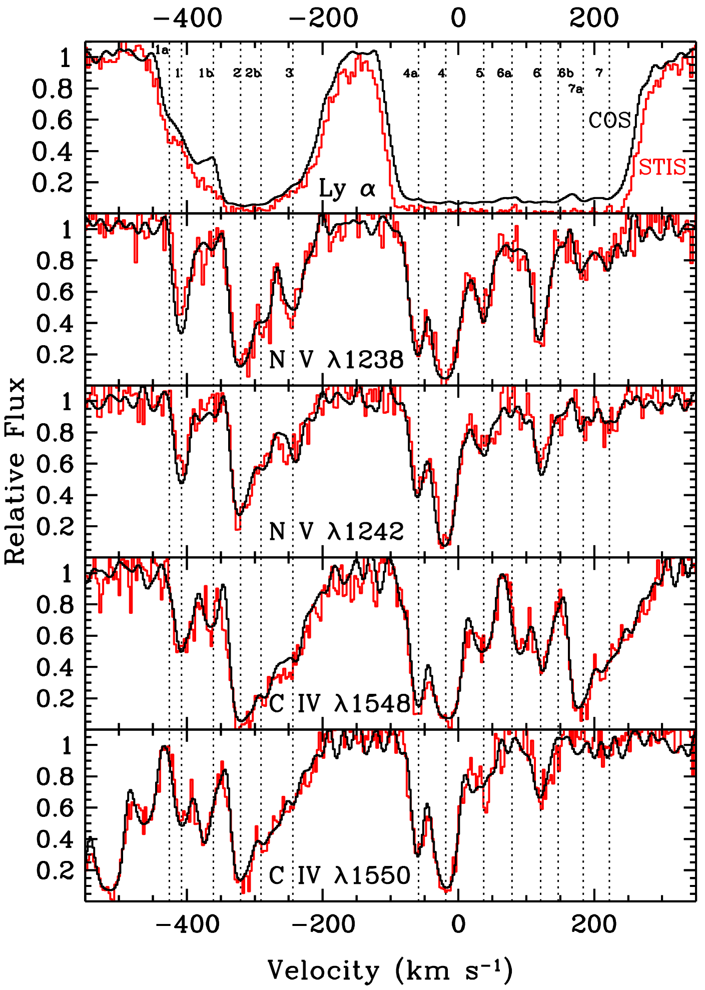

Fig. 7. Comparison of spectral features in the COS (black) and STIS (red) spectra of Mrk 509. Normalized relative fluxes are plotted as a function of velocity relative to the systemic redshift of $z = 0.034397$. The individual panels (from top to bottom) show Lyα, N v λ1238, N v λ1242, C iv λ1548, and C iv λ1550.

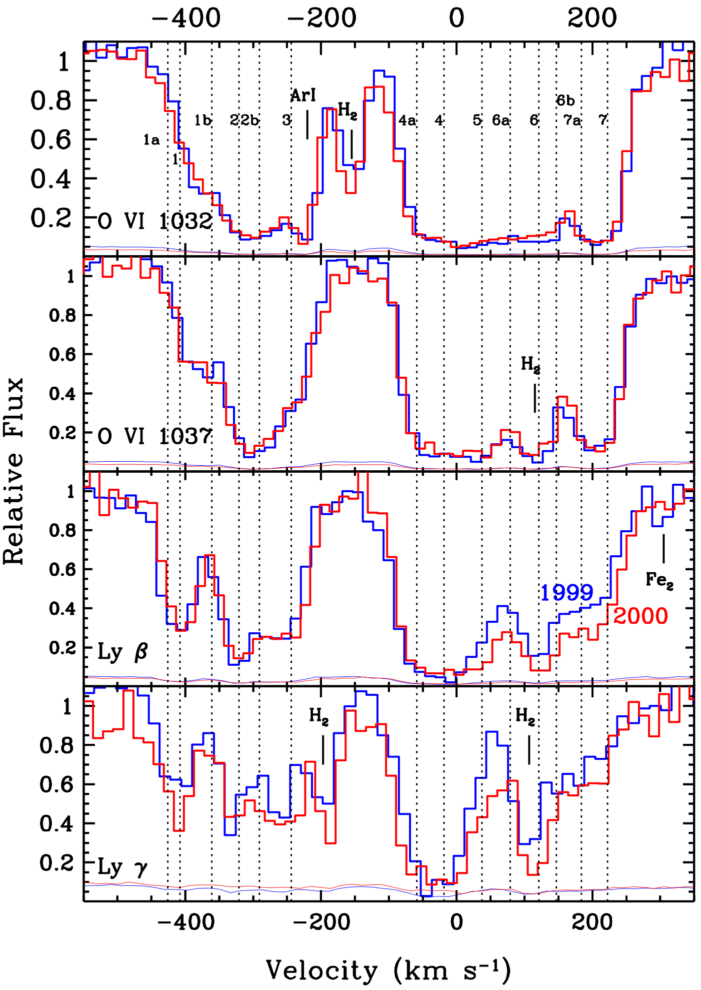

Fig. 8. Comparison of spectral features in the FUSE spectra of Mrk 509 from 1999 November (blue) and 2000 September (red). Normalized relative fluxes are plotted as a function of velocity relative to the systemic redshift of $z = 0.034397$. The individual panels (from top to bottom) show O vi λ1032, O vi λ1037, Lyβ, and Lyγ. Foreground Galactic ISM features are marked. Error vectors for each spectrum are shown as thin lines in the same color as the data.

Kraemer et al. (2003) required components with partial covering to fit the intrinsic absorption lines in their spectrum (C iv and N v as well as Lyα), as did Kriss et al. (2000) in their FUSE spectrum. If one compares the partial covering fractions among all three data sets (FUSE, STIS, and COS), one sees that COS and FUSE require similar covering fractions, and STIS somewhat less. The total depth of the O vi absorption troughs in Kriss et al. (2000) are almost directly comparable to the most highly saturated portions of the Lyα trough in the COS spectrum, with the deepest portions having ~ 92% coverage (including both the scattered light components and the partial covering factors). Note that both the COS and FUSE spectra were obtained through large apertures (2.5″ diameter and 30″ × 30″, respectively), suggesting that an extended emission component (or light from an extended scattering region) is filling in the absorption troughs. From our inspection of the COS two-dimensional images described above, since we do not resolve this component in the cross-dispersion direction, we conclude that such a region must be larger than the STIS aperture size, but smaller than the nominal COS cross-dispersion spatial resolution, which is 0.5″ at its best at a wavelength of 1600 Å (Ghavamian et al. 2010). Comparing the best-fit scattered light components from our fits to the COS and STIS spectra, 0.05 vs. 0.01, if we assume that this light is coming from a region of uniform surface brightness, the total extent of this region would be $\sqrt{5}$ times the size of the STIS aperture, or roughly 0.45″ in diameter, which is consistent with the limits in size we set from the lack of any detectable spatial extent in the COS spectrum.

This scattering region would then have a radius of ~ 150 pc. If it occupied a biconical region with a covering fraction of $\Delta\Omega/4\pi = 0.25$, following Krolik & Begelman (1986), the required Thomson optical depth τ_e to produce the scattered flux would be $\tau_e = 0.05/(\Delta\Omega/4\pi) = 0.20$, where 0.05 is the fraction of uniformly scattered light in the troughs of the COS and FUSE spectra. This gives a total column density of 3.0×10^{23} cm^{-2} for the hot gas. If it uniformly fills this volume, it has a density of 1900 cm^{-3} and a total mass of 2.0×10^8 $M_\odot$. While this is larger than the reflecting region in NGC 1068, its properties are not unreasonable for a volume filled by the outflow from the nuclear region of Mrk 509.

In addition to this scattered light component, we see differences in the depths of several absorption components in the Lyα and N v profiles. Examining Fig. 7 once again, one can see that components 1 and 1b in the COS Lyα spectrum are not as deep as in the STIS spectrum. In contrast, component 1 in the N v absorption profile is noticeably shallower in the STIS spectrum compared to the COS spectrum. More quantitatively, we can compare the column densities in Tables 9 and 10. From the FUSE Lyγ and Lyβ profiles in the velocity range of components 1b, 1, and 1a we can see that this region of velocity space is optically thin, even in the Lyα profile. Therefore, the change in the summed column density from these three components from 88×10^{12} cm^{-2} to 57×10^{12} cm^{-2} is a decrease of 35%. For N v, the column density increased from 112×10^{12} cm^{-2} to 135×10^{12} cm^{-2}. If these changes are due to a change in the ionization state of the absorbing gas, it indicates that the gas must have been in a lower ionization state in 2000, at an ionization parameter somewhat below the peak for the ionization state of N v.

Changes in absorption are also apparent when one compares the two FUSE observations, obtained roughly 10 months apart. In Fig. 8 we compare the absorption profiles in velocity space for the O vi doublet and for Lyβ and Lyγ. (One must be careful in comparing these spectra since portions of each line profile are contaminated by foreground Galactic absorption.) We have marked the contaminating features in each panel of Fig. 8. O vi is very heavily saturated at almost all velocities; we see no significant differences visually in Fig. 8. The fits in Tables 11 and 12 also show similar column densities, but, given the level of saturation in O vi, these are not reliable comparisons. In comparing the Lyβ and Lyγ profiles, however, one can see significant changes in the red side of the absorption troughs, especially for components 5, 6a, 6, 6b. There are also slight differences in the region of component 1, as we saw in comparing the COS and STIS observations. Doing a quantitative bin-by-bin comparison in velocity space over the range of components 1a, 1, and 1b, and 6a, 6, and 6b, we find that changes in the component 1 region, which primarily show up in Lyγ are significant at only the 1-σ confidence level. For components 5, 6a, 6, and 6b, however, the changes in Lyβ and Lyγ are significant at $> 3\sigma$ confidence. Summing over all of these components for H i in Tables 11 and 12, we see that the total column of H i increased from 1.16×10^{15} cm^{-2} to 1.30×10^{15} cm^{-2} from 1999 November to 2000 September. If due to a change in ionization, this is consistent with the observed decrease in continuum flux between the two observations.

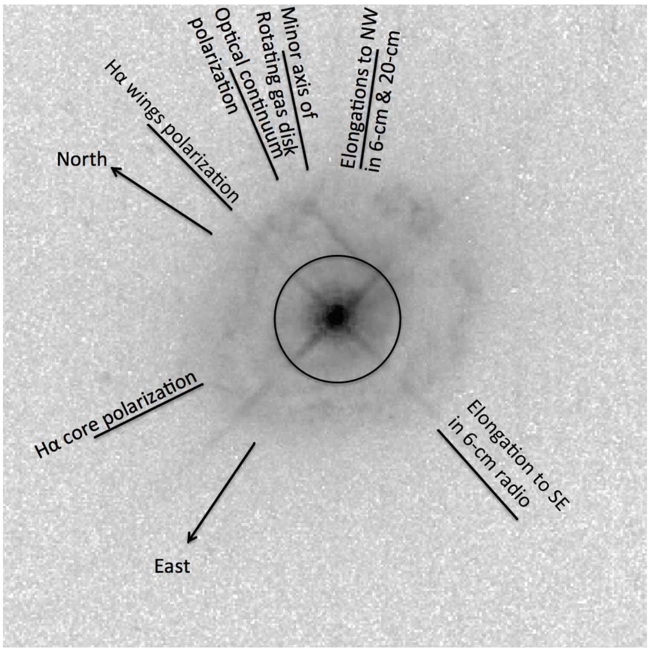

Fig. 9. HST WFPC2 image of Mrk 509 through filter F547M. The directions North and East are marked with arrows of length 2.5″. The black circle shows the placement of the 2.5″ diameter COS aperture used for our observations. Lines indicating the position angles of various features associated with the structure of Mrk 509 are indicated. The small knot at the end of the linear structure visible in the F547M image directly above the nucleus lies at a position angle (PA, measured East of North) of −42° from the nucleus. The minor axis (PA= 135°) of the low-ionization gas disk is from Phillips et al. (1983). The PA of the polarized light in the core of the Hα emission line (60°), the broad wings of Hα (168°) and the optical continuum (144°) are from Young et al. (1999). The radio structures (PA= −65° and 165°) are from Singh & Westergaard (1992). Note that extended radio emission to the NW rotates from PA= −40° to PA= −65° with increasing distance from the nucleus.

4. Discussion

4.1. The Environment of the Active Nucleus in Mrk 509

The velocities for the absorbing gas in Mrk 509 span a range from negative to positive that is atypical for AGN. When UV absorption lines are detected in low-redshift AGN, they are generally blue shifted (Crenshaw et al. 2003; Dunn et al. 2007). This is also true of higher redshift quasars (Weymann et al. 1979; Ganguly et al. 2001; Misawa et al. 2007), although Weymann et al. (1979) did suggest that systems with red-shifted absorption lines could be associated with neighboring galaxies in clusters. However, given the significant blue shifts of the UV emission lines often used to define the quasar redshift, such redshifted systems could well be blueshifted relative to the systemic velocities of the host galaxies. In fact, Ganguly et al. (2001) finds that the distribution of associated narrow-line absorbers in QSOs peaks around the UV emission-line velocity. Nevertheless, one might expect to find gas with random motions, both blue- and red-shifted, relative to the host galaxy intercepting our line of sight either within the host galaxy itself or associated with its neighbors. Indeed, one component of the absorption in the Seyfert 1 galaxy Mrk 279 has a positive velocity of +90 km s^{-1}, and Scott et al. (2004) have suggested that it is interstellar material in the host galaxy, or gas from a recent encounter with a close companion, perhaps similar to a high-velocity cloud (HVC) in our own Milky Way.

Since our absorption-line observations only probe gas that is along the line of sight, taking a broader view of the environment of the active nucleus in Mrk 509 should be helpful. The optical imaging and two-dimensional optical spectroscopy of Phillips et al. (1983) reveal a compact host, perhaps of type S0. The spectroscopy shows kinematically distinct low-ionization and high-ionization emission-line components. The low-ionization gas covers the face of the galaxy and rotates as a disk about an axis at a position angle (PA, measured East of North) of −45°. The high-ionization gas also extends to more than 10″ from the nucleus, and it is mostly blueshifted, with velocities as high as −200 km s^{-1}, although there are also regions SE of the nucleus with positive velocities. Radio images of Mrk 509 show elongation and extensions to both the NE and the SW (Singh & Westergaard 1992).

To illustrate these features on the spatial scale of our HST observations, we have retrieved the WFPC2 F547M image of Mrk 509 obtained by Bentz et al. (2009) from the MAST archive. We used MultiDrizzle (Fruchter et al. 2009) to combine the longest PC exposures (with exposure times of 60 s, 160 s, and 300 s) and eliminate cosmic rays. Figure 9 shows the resultant image (covering the inner 4 kpc of Mrk 509). Note that this image does not capture the full extent of Mrk 509. The 2.5″-diameter COS aperture covers only the central 870 pc of Mrk 509, while the most prominent features in the HST image, possibly an irregular starburst ring, have an outer radius of < 2 kpc. If this ring-like feature is due to recent star formation, this may be the source of ionization for the low-ionization rotating disk in the spectroscopy of Phillips et al. (1983). There is also an unusual, linear feature to the NE, which is not aligned with the nucleus, although it lies in the general direction of the elongations to the NW in the radio maps. Deep ground-based CCD images of Mrk 509 show an amorphous optical morphology (MacKenty 1990) with a broad extension to the SE in the same direction as the elongation in the 6-cm radio image of Singh & Westergaard (1992). Although the light is highly concentrated, MacKenty (1990) traces an exponential disk out to a radius of more than 30 kpc.

In addition to this macroscopic view of the nuclear region, optical spectropolarimetric observations have probed structures that are unresolved in the optical or radio images. Optical spectropolarimetry of Mrk 509 suggests that there are multiple scattering regions, each consistent with various aspects of the unified model of AGN (Young 2000). The optical continuum is polarized at PA=139–154°, along the same direction as the inner portions of the 6-cm and 20-cm radio images (Singh & Westergaard 1992). The polarization is also variable (Young et al. 1999), and Young (2000) identified this as radiation scattered from the accretion disk. The Hα emission line exhibits more complexity in its polarization. The core is polarized at PA=60°, nearly perpendicular to the radio jet, as observed in Type II AGN, where the scattering surface is the mirror of hot electrons in the cone along the radio axis, perpendicular to the plane of the obscuring torus. The wings of Hα are polarized at PA=168°, similar to, but not quite aligned with the inner radio jet. Figure 9 shows these orientations relative to other structures in Mrk 509.

As we noted in §3.4, the COS and FUSE spectra show significantly more residual light at the bottoms of the intrinsic absorption-line troughs than does the STIS spectrum. Since COS and FUSE used larger apertures, we argued that much of this light was scattered light, primarily from a region less than 0.44445″ in diameter surrounding the active nucleus. (This scattered light is from a much smaller region than the broad Balmer emission that Mediavilla et al. (1998) detected using two-dimensional spectroscopy over a region of $\sim 8''$ surrounding the nucleus, which they interpret as scattered light from the AGN.) A distance of 0.225″ corresponds to a radial distance of < 150 pc, which would place it in the typical region associated with reflective hot-electron mirrors in Type II AGN, as we noted in §3.4. This is consistent with the polarization component seen in the core of the Hα emission line that is polarized perpendicularly to the radio axis. The amount of scattered light we see, approximately 5% of the total flux, is also typical of the amount of scattered light seen in Type II AGN like NGC 1068 (Miller et al. 1991; Antonucci 1993).

Thus our line of sight to the nucleus in Mrk 509 may pass through a complicated mix of components. Based on the kinematics and physical characteristics of the absorption components revealed by our spectrum, we will try to link the absorption components to the various features in Mrk 509.

4.2. Characterizing the Absorbers

In this paper we take a kinematic approach to identifying and characterizing the absorbers in Mrk 509 (as opposed to the ionization-state approach used by Detmers et al. 2011 and Ebrero et al. 2011). As in Ebrero et al. (2011), our discussion is a preliminary assessment of the properties of the absorbers. A more comprehensive analysis of the X-ray and UV properties of the absorbing gas is deferred to a future paper (Ebrero, in preps.).

On the largest velocity scales, the intrinsic absorption in Mrk 509 can be characterized by two main troughs. The most blue-shifted trough, extending from $-200\ \mathrm{km\,s^{-1}}$ to $-450\ \mathrm{km\,s^{-1}}$, corresponds to the velocities of the most prominent blue-shifted absorption component in the RGS spectrum ($-319\ \mathrm{km\,s^{-1}}$; Detmers et al. 2011) and the *Chandra* spectrum ($-196\ \mathrm{km\,s^{-1}}$; Ebrero et al. 2011). (This velocity offset between the RGS and LETGS results is not significant, and it lies within the range of systematic errors in the relative RGS and LETGS wavelength scales as discussed by Kaastra et al. 2011a and Ebrero et al. 2011.) Given the variability we have seen in portions of this trough and its blueshift, we identify this trough as an outflow from the AGN.

The other main absorption trough in Mrk 509 extends from $-100\ \mathrm{km\,s^{-1}}$ to $+250\ \mathrm{km\,s^{-1}}$. This also matches the kinematics of the other main absorption component detected in the X-ray spectra, with velocities measured in the RGS spectrum of $-13\ \mathrm{km\,s^{-1}}$ (Detmers et al. 2011) and of $+73\ \mathrm{km\,s^{-1}}$ in the *Chandra* spectrum (Ebrero et al. 2011). The ionization level in the X-ray for this component is lower, and this gas is not in pressure equilibrium with the gas in the blue-shifted absorption trough (Ebrero et al. 2011). As we discuss below, the components in this trough may arise in several distinctly different regions of Mrk 509. The higher spectral resolution of our UV spectrum permits us to dissect these absorption features in greater detail, so we now discuss the properties of individual components that we have identified in the UV absorption spectrum.

4.2.1. Components 1a, 1, and 1b

Component 1a is detected only in the far wing of the Lyα absorption trough. There is a distinct depression here that is not seen in the profiles of any of the other absorption lines, including O vi. This suggests that the gas here may be very highly ionized, perhaps representing the only indication in the UV of a more extensive outflow at higher velocities that is seen in some of the most highly ionized X-ray absorption features (Detmers et al. 2011; Ebrero et al. 2011).

Components 1 and 1b show definite evidence of variability from comparing the STIS and COS observations. Both vary in Lyα, and component 1 varies in N v as we discussed in §3.4. Although more closely spaced in time, the FUSE observations do not permit us to set any interesting limits on the density or location of the gas in these components. These components may have varied between the two FUSE observations, but not at a level of significance that permits us to infer densities or distances. The variations in N v and Lyα are consistent with ionization changes in response to a decrease in the continuum flux. Recombination times for hydrogen are too slow to permit us to set any interesting limits on the density. However, N v recombines nearly two orders of magnitude faster, and it provides greater leverage in sensing the density of the absorbing medium. Following Krolik & Kriss (1995) and Nicastro et al. (1999), recombination and ionization time scales depend not only on the density, but also on the relative populations of the ionization states involved: $t_{rec} = (n_i/n_{i+1})/(n_e\alpha_{rec})$. Using the photoionization model for the Mrk 509 absorbers from Kraemer et al. (2003), component 1 has an ionization parameter $\log \xi = 0.67$ (where $\xi = L_{ion}/(nr^2)$). At this level, the ionization fraction for N v is ∼ 0.4, and the relative equality of populations among the neighboring ionization states of nitrogen makes ionization and recombination timescales similar (Nicastro et al. 1999). For $\alpha_{rec} = 8.96 \times 10^{-12}\ cm^3\ s^{-1}$ (Nahar 2006) at a temperature of 20,000 K, and a time between the STIS and COS observations of 2.733×10^8 s, we get a lower limit on the density of $n_e > 160\ \mathrm{cm}^{-3}$. Since we are using the photoionization models of Kraemer et al. (2003), we use an ionizing luminosity from their SED in Yaqoob et al. (2003), $L_{ion} = 7.0 \times 10^{44}$ ergs s^{-1}. Together with the ionization parameter $\log\xi = 0.67$, this gives an upper limit on the distance of $r < 250$ pc.

Component 1 is well defined in both N v and C iv, but in Lyα and O vi it is merely part of a smoothly varying trough that runs from the deepest point in components 2 and 2b. As modeled by Kraemer et al. (2003) (who only used the STIS data), this trough has only moderate ionization, probably even lower than what they model since they grossly overpredict the amount of O vi that should be present at this velocity. (Their trough at −420 km s^{-1} is three times deeper than the observed O vi λ1032 absorption in the FUSE spectrum at this velocity.) In fact, as we discussed in §3.4, given the relative character of the variability in Lyα and N v, the ionization state of this feature is below the peak in ionization for N v. Component 1b appears to have higher ionization since it is strong in O vi but very indistinct in N v. Although moderately strong in Lyα, it is also weaker than component 1. If either of these components are associated with the X-ray portion of the outflow (which they do not match in detail kinematically), they are likely to be higher-density, lower-ionization clumps embedded in a more tenuous, highly ionized outflow.

4.2.2. Components 2 and 2b

Components 2 and 2b represent the deepest portions of the blue half of the absorption trough in the Mrk 509 spectrum. Kinematically, these components are the closest match to one of the major components detected in the X-ray spectrum of Mrk 509. In the *XMM-Newton*/RGS spectrum, component 2 of Detmers et al. (2011) is almost an exact match in velocity to UV component 2 (−319 km s^{-1} vs. −321 km s^{-1}, respectively). The ionization state of the gas detected in the UV absorption lines, however, is not particularly high, and its total column density is less than that seen in the X-ray. Again, this may be an example of a higher-density, lower-ionization clump embedded in the more highly ionized outflow seen in the X-ray.

4.2.3. Component 3

Component 3 is the closest match in velocity to Component 2 of the *Chandra* LETGS spectrum (Ebrero et al. 2011), but in the UV it too has rather low ionization, similar in character to UV component 1. As with the previous components, this gas detected in the UV is likely to be a higher-density clump embedded in more highly ionized outflowing gas.

4.2.4. Component 4a

Component 4a, first identified by Kraemer et al. (2003), shows up most clearly in N v and C iv. In velocity it is close to component 1 identified in the RGS spectrum by Detmers et al. (2011). Its modest outflow velocity could suggest an association with the base of the outflowing wind in Mrk 509. However, like all the components above, it is rather low in ionization, and its column density is lower than that seen in the X-ray absorber. It is probably not directly associated with the X-ray absorbing gas.

4.2.5. Component 4

Perhaps the easiest component to characterize is #4. This absorber has the lowest ionization state of any of the components. It is the only one in which Si iv is detected, and it has the strongest C iii absorption in the original FUSE spectrum of Kriss et al. (2000). Its velocity of ∼ −22 km s^{-1} is the closest to our adopted systemic redshift for Mrk 509. Given the high column densities, relatively low ionization state and velocity coincidence, it is likely that this component is the interstellar medium of the Mrk 509 host galaxy. Phillips et al. (1983) find a systemic velocity for the rotating low-ionization gas disk in their observations that is in good agreement with the velocity of the [O iii] line-center velocity which they adopted as the systemic velocity of the host galaxy. To within their errors of ±30 km s^{-1}, all of these velocities are consistent with the velocity we measure for component 4. Kraemer et al. (2003) find that the broad range of UV ionization states present at this velocity requires more than one component in a photoionization model solution. Component 4 has the closest match in velocity to component 1 identified in the RGS spectrum by Detmers et al. (2011). Within the errors of the *Chandra* spectrum, Component 4 may also be associated with component 1 from the LETGS spectrum (Ebrero et al. 2011). Given its low ionization parameter, Ebrero et al. (2011) suggest that this X-ray absorption may be associated with the ISM or halo of the host galaxy of Mrk 509.

4.2.6. Component 5

Component 5 is similar in character to Component 4, but it has lower overall column density and slightly higher ionization. Its slightly positive velocity is a good match to component 1 in the LETGS spectrum. Highly ionized gas at this velocity is also seen in the three-dimensional spectroscopy of Phillips et al. (1983), and it is within the velocity profile of the echelle spectrum of [O iii] in the nuclear region of Mrk 509. It appears to have varied in strength in H i between the two FUSE observations. As it is difficult to disentangle this component's variations from those of components 6a, 6, and 6b, we discuss the implications of this variation in the next subsection.

4.2.7. Components 6a, 6, and 6b

Although component 6 has a positive velocity, this does not preclude it from an association with the active nucleus in Mrk 509. In fact, if one examines the [O iii] echelle spectrum of the nuclear region in Mrk 509 in Fig. 3 of Phillips et al. (1983), one can see that the actual peak of the line is at a positive velocity of +120 km s^{-1}, matching our velocity for absorption in component 6. The kinematics of X-ray-heated winds modeled by Balsara & Krolik (1993) shows that portions of the flow that are evaporated off the inner edge of the obscuring torus can be captured by the central black hole. This results in streamlines with positive, inflow velocities.

The variability in H I absorption we see over the 10 months between the two FUSE observations suggests a close relationship to the active nucleus for components 5 and 6, and, as for Component 1, it allows us to set an upper limit on the distance of this gas from the central engine. From 1999 November to 2000 September, over an interval of 303 days, the continuum flux from Mrk 509 dropped by 30%, and the hydrogen column density in components 5 and 6 increased by 14%, as we showed in §3.4. This gives us an upper limit on the recombination time for the gas, and hence a lower limit on the density. Again using the photoionization model from Kraemer et al. (2003), component 6 has an ionization parameter $\log \xi = 0.71$, and an ionization fraction for hydrogen of 2.3×10^{-5}. For a time interval between the two FUSE observations of 2.62×10^{7} s, and $\alpha_{\rm rec} = 1.43 \times 10^{-13}\ {\rm cm}^3\ {\rm s}^{-1}$ (Osterbrock & Ferland 2006) at a temperature of 20,000 K, we get a limit on the density of $n_e > 6.0\ {\rm cm}^{-3}$. The ionizing luminosity of $L_{\rm ion} = 7.0 \times 10^{44}$ ergs s^{-1} together with the ionization parameter $\log\xi = 0.71$, gives an upper limit on the distance of $r < 1.5$ kpc. So, component 6 is definitely within the confines of the host galaxy, and likely in the near vicinity of the nucleus.

4.2.8. Components 7a and 7

Component 7 at +219 km s^{-1}, from its velocity, is not outflowing, but infalling to Mrk 509. Component 7a is strongly blended with #7 in O VI and Lyα; it only shows up as a kinematically independent feature in N V. Neither component shows any significant variability either between the two FUSE observations in 1999 and 2000, or between the longer interval between STIS and COS from 2001 to 2009. Given that it is optically thin in N V, C IV, and Lyα, this lack of variability is not being masked by saturation effects that limit our ability to see variations in other components. Based on just the qualitative appearance of the UV spectra, this is the highest ionization parameter trough in the whole spectrum—O VI is very strong, N V is present, and C IV is not detectable. The stacked RGS spectrum at these velocities (Detmers et al. 2011) does not reveal absorption in O VI Kα, although the upper limits are consistent with the FUSE spectrum. So, even though the ionization level exhibited in the UV is high, it is still not as high as the blue-shifted trough in the X-ray spectrum. Kraemer et al. (2003) and Kriss et al. (2000) found their highest ionization parameters for this component as well.

We suggest that components 7 and 7a might be similar to HVC complexes seen in our own galaxy, except that the ionization of these clouds in Mrk 509 would be completely dominated by the radiation from the active nucleus rather than the extragalactic background radiation and starlight from the galaxy. These clouds may be infalling extragalactic material, or they may be tidal material stripped from an encounter with a companion in the past. Although Mrk 509 does not have an obvious interacting companion, its disturbed outer isophotes (MacKenty 1990) suggest there may have been an encounter in the more distant past. Thom et al. (2008) find that HVC Complex C in the Milky Way has an average density $\log n \sim -2.5$, dimensions 3×15 kpc, a distance of 10 ± 2.5 kpc, and a total mass of $8.2^{+4.6}_{-2.6} \times 10^{6}\ M_{\odot}$. If components 7 and 7a in Mrk 509 have roughly similar densities of $n = 0.01\ {\rm cm}^{-3}$, then we can use the photoionization results of Kraemer et al. (2003) to estimate their size and distance from the nucleus of Mrk 509. Kraemer et al. (2003) give a total column density of $N_H = 4 \times 10^{19}\ {\rm cm}^{-2}$ for component 7, which implies a size (as a cube) of $1.3(0.01\ {\rm cm}^{-3}/n)$ kpc. For their quoted ionization parameter of $\log \xi = 1.33$, and an ionizing luminosity of $L_{\rm ion} = 7.0 \times 10^{44}$ ergs s^{-1}, the distance from the center of Mrk 509 is $19\ (0.01\ {\rm cm}^{-3}/n)^{0.5}$ kpc. This is just about right for a structure comparable to a Milky Way HVC. For a density this low and ionization this high, the recombination time for H I in components 7a and 7 would be $80(0.01\ {\rm cm}^{-3}/n)$ years, so the lack of variability in our observations is consistent with this hypothesis.

4.2.9. Smoothly distributed gas in the outflow

While we have characterized the absorption features in Mrk 509 in terms of discrete kinematic components, the smoothly varying profiles of the Lyα and O VI absorption in the blue-shifted outflow trough (see Fig. 5) suggest that additional gas may be present that is smoothly distributed over a range in velocities. The tail to higher velocities observed as component 1a in Lyα may be a part of this distribution. If this smoothly distributed gas is very highly ionized, one might expect that the only traces remaining in the UV absorption spectrum would be the most highly ionized species, like O VI, or the most abundant ones, like H I. This more smoothly distributed, highly ionized gas could be the counterpart of the features detected in the RGS and LETGS X-ray spectra.

The discrete UV absorption components we have identified show up most clearly in N V and C IV. As noted in §3.3, these often do not precisely align with similar features in O VI and Lyα. For example, in the region surrounding component 1b, there is little C IV and N V absorption, but moderate depth in O VI and the hydrogen lines, although it is a local minimum in H I. The lower ionization, more discrete components we observe in N V and C IV could be dense, lower-ionization clumps embedded in this flow, or clouds in the interstellar medium of Mrk 509 that are being entrained in the flow. As shown by Ebrero et al. (2011), these lower-ionization components are not in pressure equilibrium with the other X-ray absorbing components. Such discrete clouds with similar kinematics are spatially resolved and observed in the nearest AGN, e.g., NGC 4151 (Das et al. 2005) and NGC 1068 (Das et al. 2006, 2007). This outflowing gas is also visible in the three dimensional spectroscopy of Phillips et al. (1983).

4.3. Thermal Winds vs. Disk Winds

Disk winds are a popular explanation for outflows from AGN (Königl & Kartje 1994; Murray & Chiang 1995; Elvis 2000; Proga et al. 2000; Richards et al. 2010; Fukumura et al. 2010). For the high velocities observed in broad-absorption-line (BAL) QSOs, an origin for the wind from the accretion disk deep in the potential well of the central black hole is a natural inference. For the low velocities we observe in Mrk 509, it is not so clear. Kraemer et al. (2003) summarizes the problems faced in trying to explain the outflow in Mrk 509 with a disk wind. Briefly, Mrk 509 is likely to be observed nearly face on to the accretion disk based on the polarized flux in the broad wings of Hα that is polarized parallel to the radio jet, suggesting an origin in scattering from the face of the accretion disk (Young et al. 1999; Young 2000). Since disk winds roughly lie in the plane of the disk, the flow would be predominantly perpendicular to our line of sight. This can explain the low velocities since most of the motion would be transverse to our line of sight, but it makes it difficult to explain the near-unity covering factors of the absorbers if the UV continuum is produced interior to the launch point of the wind.

The modest velocities of hundreds of km s^{-1} we observe here are more characteristic of thermal winds produced in the AGN environment. Irradiation of the obscuring torus in an AGN by the nuclear flux produces material that fills the cone above the torus and flows outward at velocities of hundreds of km s^{-1}, typical of the sound speed in the gas (Balsara & Krolik 1993; Krolik & Kriss 1995, 2001). The presence of some redshifted components is also consistent with portions of an X-ray-heated wind that are captured by the central black hole (Balsara & Krolik 1993). These winds are also expected to have multiple phases of gas as the surface of the torus is ablated by the radiation from the central engine (Krolik & Kriss 1995, 2001). The most highly ionized portions of this flow can produce the X-ray absorption. The dense part of the wind near the base of the ionization cone may be the slightly extended scattering region producing the extra flux we see in the bottoms of the absorption troughs and also produce the polarization seen in the core of the Hα emission line. As we noted in the prior section, the lower-ionization UV absorption components could be denser clumps embedded in this flow. The extended high-ionization [O III] emission outflowing from the nuclear region and studied by Phillips et al. (1983) could be analogous to the discrete clouds imaged with HST in nearby AGN that show similar kinematics.

5. Conclusions

We have presented HST/COS observations of the Seyfert 1 galaxy Mrk 509 obtained as part of an extensive multiwavelength campaign (Kaastra et al. 2011b) on this galaxy in late 2009. Our UV spectra were obtained simultaneously with *Chandra* LETGS spectra (Ebrero et al. 2011). The campaign also included immediately prior observations with *XMM-Newton*, Swift, and INTEGRAL. Our spectra cover the 1155–1760 Å wavelength range at a resolution of $\sim$ 15 km s^{-1}, and they are the highest signal-to-noise observations to date of the intrinsic absorption components of Mrk 509. This enables us to trace additional complexity in the absorption troughs compared to prior STIS observations (Kraemer et al. 2003). As part of our analysis, we have also examined archival FUSE observations, which provide additional information on variability characteristics of the absorbers.

In our COS spectra we identify a total of 14 kinematic components. Six of these are blends that represent subcomponents of previously known features. The most blueshifted portions of the Lyα absorption trough (components 1 and 1b) show a significant decrease in column density compared to prior STIS observations. At the same time, component 1 in N V increased in strength compared to the STIS observations. Using recombination timescale arguments, the variation in the N V column density allows us to set a lower limit on the gas density of > 160 cm^{-3}, and an upper limit on the distance of < 250 pc for this most blue-shifted component. We also detect variability between the two FUSE observations from 1999 November (Kriss et al. 2000) to 2000 September in component 6 at a positive velocity of +120 km s^{-1}, which corresponds to the peak of the [O III] emission-line profile from the echelle spectrum of Phillips et al. (1983). Based on the recombination time, we set a limit on the density of this component of > 6 cm^{-3}, and set an upper limit on its distance from the nucleus at < 1.5 kpc.

The COS spectra also show greater residual light at the bottoms of the absorption troughs relative to the STIS spectrum. The fraction of residual light seen in COS is comparable to that seen in the FUSE spectra. We attribute this residual light to scattering from an extended region near the nucleus, which is consistent with the larger apertures used for the COS and FUSE observations relative to the STIS spectrum. Analysis of the cross-dispersion profile in the COS spectrum limits the spatial extent of this scattering region to $< 0.5''$, or < 170 pc. Scattering from such a region would be consistent with electron scattering from the base of an ionization cone in Mrk 509, and it would explain the polarization in the core of Hα (Young et al. 1999) which is observed to be perpendicular to the radio jet (Singh & Westergaard 1992).

The velocities of the two main absorption troughs roughly correspond to the kinematics of the detected X-ray absorption. The UV absorption in Mrk 509 arises from a variety of sources. The lowest-velocity absorption trough covers a velocity range of −100 km s^{-1} to +250 km s^{-1}. The deepest portion of this trough in the UV is at the systemic velocity of Mrk 509, and it has the lowest ionization. This is also true for the X-ray absorption. We attribute this portion of the absorption to the interstellar medium or galactic halo of Mrk 509. The most redshifted portion of the trough has characteristics comparable to the high-velocity cloud Complex C in our own Milky Way (Thom et al. 2008). At a density of 0.01 cm^{-3} (which we can only assume, not measure), it would have a size of roughly 1.3 kpc at a distance of 19 kpc from the center of Mrk 509.

The most blue-shifted absorption trough in Mrk 509 is an outflow from the active nucleus. The velocities in this trough of −200 km s^{-1} to −450 km s^{-1} correspond to the most highly ionized portion of the X-ray absorbing gas (Detmers et al. 2011; Ebrero et al. 2011), and they overlap with the extended emission from high-ionization gas that covers the face of Mrk 509 in the three-dimensional spectroscopy of Phillips et al. (1983). The outflow velocities, embedded clumps of lower ionization gas, the presence of an extended scattering region, and the extended outflowing emission seen in [O III] (Phillips et al. 1983) are all consistent with an origin in a multiphase thermal wind produced by the irradiation of an obscuring torus by the active nucleus.

Acknowledgements. This work was supported by NASA through grants for HST program number 12022 from the Space Telescope Science Institute, which is operated by the Association of Universities for Research in Astronomy, Incorporated, under NASA contract NAS5-26555, *XMM-Newton* grant NNX09AR01G from Goddard Space Flight Center. SRON is supported financially by NWO, the Netherlands Organization for Scientific Research. KCS acknowledges the support of Comité Mixto ESO - Gobierno de Chile. SB acknowledges financial support from contract ASI-INAF n. I/088/06/0. EB was supported by a grant from the Israel Science Foundation. PoP acknowledges financial support from the GDR PCHE in France and from the CNES French national space agency. GP acknowledges support via an EU Marie Curie Intra-European Fellowship under contract no. FP7-PEOPLE-2009-IEF-254279.

References

Ake, T., Massa, D., Beland, S., et al. 2010, in HST Calibration Workshop, ed. S.Deustua & C. Oliveira (Baltimore: STScI), in press
Aloisi, A., Bohlin, R., & Quijano, J. K. 2007, New On-Orbit Sensitivity Calibration for All STIS Echelle Modes, Tech. Rep. Instrument Science Report STIS 2007-01, STScI, Baltimore
Antonucci, R. 1993, ARA&A, 31, 473
Arav, N., Gabel, J. R., Korista, K. T., et al. 2007, ApJ, 658, 829
Arav, N., Korista, K. T., & de Kool, M. 2002, ApJ, 566, 699
Arav, N., Korista, K. T., de Kool, M., Junkkarinen, V. T., & Begelman, M. C. 1999, ApJ, 516, 27
Balsara, D. S. & Krolik, J. H. 1993, ApJ, 402, 109
Barai, P., Martel, H., & Germain, J. 2011, ApJ, 727, 54
Barlow, T. A. & Sargent, W. L. W. 1997, AJ, 113, 136
Barth, A. J., Martini, P., Nelson, C. H., & Ho, L. C. 2003, ApJ, 594, L95

Bentz, M. C., Peterson, B. M., Pogge, R. W., & Vestergaard, M. 2009, ApJ, 694, L166

Cappi, M., Tombesi, F., Bianchi, S., et al. 2009, A&A, 504, 401

Cardelli, J. A., Clayton, G. C., & Mathis, J. S. 1989, ApJ, 345, 245

Cavaliere, A., Lapi, A., & Menci, N. 2002, ApJ, 581, L1

Costantini, E., Kaastra, J. S., Arav, N., et al. 2007, A&A, 461, 121

Crenshaw, D. M., Kraemer, S. B., & George, I. M. 2003, ARA&A, 41, 117

Das, V., Crenshaw, D. M., Hutchings, J. B., et al. 2005, AJ, 130, 945

Das, V., Crenshaw, D. M., & Kraemer, S. B. 2007, ApJ, 656, 699

Das, V., Crenshaw, D. M., Kraemer, S. B., & Deo, R. P. 2006, AJ, 132, 620

Detmers, R. G., Kaastra, J. S., Steenbrugge, K. C., et al. 2011, A&A, in press

Di Matteo, T., Springel, V., & Hernquist, L. 2005, Nature, 433, 604

Dietrich, M., Hamann, F., Shields, J. C., et al. 2003, ApJ, 589, 722

Dixon, W. V. D., Oliveira, C., Massa, D., et al. 2010, Cosmic Origins Spectrograph Instrument Handbook, Version 3.0, Tech. rep., STScI, Baltimore

Dunn, J. P., Crenshaw, D. M., Kraemer, S. B., & Gabel, J. R. 2007, AJ, 134, 1061

Ebrero, J., Kriss, G. A., Kaastra, J. S., et al. 2011, A&A, submitted

Edmonds, D., Arav, N., Borguet, B., Dunn, J. P., & Penton, S. 2011, ApJ, submitted

Elvis, M. 2000, ApJ, 545, 63

Freudling, W., Corbin, M. R., & Korista, K. T. 2003, ApJ, 587, L67

Fruchter, A., Sosey, M., Hack, W., et al. 2009, The MultiDrizzle Handbook, Version 3.0, Tech. rep., STScI, Baltimore

Fukumura, K., Kazanas, D., Contopoulos, I., & Behar, E. 2010, ApJ, 715, 636

Furlanetto, S. R. & Loeb, A. 2001, ApJ, 556, 619

Gabel, J. R., Arav, N., Kaastra, J. S., et al. 2005a, ApJ, 623, 85

Gabel, J. R., Crenshaw, D. M., Kraemer, S. B., et al. 2003, ApJ, 583, 178

Gabel, J. R., Kraemer, S. B., Crenshaw, D. M., et al. 2005b, ApJ, 631, 741

Ganguly, R., Bond, N. A., Charlton, J. C., et al. 2001, ApJ, 549, 133

Ganguly, R., Eracleous, M., Charlton, J. C., & Churchill, C. W. 1999, AJ, 117, 2594

Germain, J., Barai, P., & Martel, H. 2009, ApJ, 704, 1002

Ghavamian, P., Aloisi, A., Lennon, D., et al. 2009, Preliminary Characterization of the Post- Launch Line Spread Function of COS, Tech. Rep. Instrument Science Report COS 2009-01(v1), STScI, Baltimore

Ghavamian, P., Froning, C., Osterman, S., Keyes, C. D., & Sahnow, D. 2010, COS FUV External Spectroscopic Performance, Tech. Rep. Instrument Science Report COS 2010-09(v1), STScI, Baltimore

Granato, G. L., De Zotti, G., Silva, L., Bressan, A., & Danese, L. 2004, ApJ, 600, 580

Hamann, F., Barlow, T. A., Junkkarinen, V., & Burbidge, E. M. 1997, ApJ, 478, 80

Hamann, F. & Ferland, G. 1993, ApJ, 418, 11

Hamann, F. & Ferland, G. 1999, ARA&A, 37, 487

Hamann, F. W., Barlow, T. A., Chaffee, F. C., Foltz, C. B., & Weymann, R. J. 2001, ApJ, 550, 142

Hopkins, P. F., Cox, T. J., Kereš, D., & Hernquist, L. 2008, ApJS, 175, 390

Hopkins, P. F. & Elvis, M. 2010, MNRAS, 401, 7

Huchra, J., Latham, D. W., da Costa, L. N., Pellegrini, P. S., & Willmer, C. N. A. 1993, AJ, 105, 1637

Juarez, Y., Maiolino, R., Mujica, R., et al. 2009, A&A, 494, L25

Kaastra, J., de Vries, C., Steenbrugge, K., et al. 2011a, A&A, in press

Kaastra, J., Petrucci, P., Cappi, M., et al. 2011b, A&A, in press

Königl, A. & Kartje, J. F. 1994, ApJ, 434, 446

Kopylov, I. M., Lipovetskii, V. A., Pronik, V. I., & Chuvaev, K. K. 1974, Astrophysics, 10, 305

Kraemer, S. B., Crenshaw, D. M., Gabel, J. R., et al. 2006, ApJS, 167, 161

Kraemer, S. B., Crenshaw, D. M., Yaqoob, T., et al. 2003, ApJ, 582, 125

Kriss, G. 1994, Astronomical Data Analysis Software and Systems, 3, 437

Kriss, G. A. 2011, Improved Medium Resolution Line Spread Functions for COS FUV Spectra, Tech. Rep. Instrument Science Report COS 2011-01(v1), STScI, Baltimore

Kriss, G. A., Green, R. F., Brotherton, M., et al. 2000, ApJ, 538, L17

Krolik, J. H. & Begelman, M. C. 1986, ApJ, 308, L55

Krolik, J. H. & Kriss, G. A. 1995, ApJ, 447, 512

Krolik, J. H. & Kriss, G. A. 2001, ApJ, 561, 684

MacKenty, J. W. 1990, ApJS, 72, 231

Massa, D., Keyes, C., Penton, S., Bohlin, R., & Froning, C. 2010, SMOV Absolute Flux Calibration of the COS FUV Modes, Tech. Rep. Instrument Science Report COS 2010-02(v1), STScI, Baltimore

Mediavilla, E., Arribas, S., Garcia-Lorenzo, B., & del Burgo, C. 1998, ApJ, 494, L9+

Mehdipour, M., Branduardi-Raymont, G., Kaastra, J. S., et al. 2011, A&A, submitted

Miller, J. S., Goodrich, R. W., & Mathews, W. G. 1991, ApJ, 378, 47

Misawa, T., Charlton, J. C., Eracleous, M., et al. 2007, ApJS, 171, 1

Moos, H. W., Cash, W. C., Cowie, L. L., et al. 2000, ApJ, 538, L1

Murphy, E. M., Lockman, F. J., Laor, A., & Elvis, M. 1996, ApJS, 105, 369

Murray, N. & Chiang, J. 1995, ApJ, 454, L105

Nahar, S. N. 2006, ApJS, 164, 280

Nicastro, F., Fiore, F., & Matt, G. 1999, ApJ, 517, 108

Osten, R. A., Ghavamian, P., Niemi, S., et al. 2010, Early Results from the COS Spectroscopic Sensitivity Monitoring Programs, Tech. Rep. Instrument Science Report COS 2010-15 (v1), STScI, Baltimore

Osterbrock, D. E. & Ferland, G. J. 2006, Astrophysics of gaseous nebulae and active galactic nuclei (Mill Valley: University Science Books)

Pentericci, L., Fan, X., Rix, H., et al. 2002, AJ, 123, 2151

Penton, S. V., Stocke, J. T., & Shull, J. M. 2000, ApJS, 130, 121

Phillips, M. M., Baldwin, J. A., Atwood, B., & Carswell, R. F. 1983, ApJ, 274, 558

Proga, D., Stone, J. M., & Kallman, T. R. 2000, ApJ, 543, 686

Richards, G. T., Kruczek, N. E., Gallagher, S. C., et al. 2010, ArXiv e-prints, 1011.2282

Ruiz, J. R., Crenshaw, D. M., Kraemer, S. B., et al. 2005, AJ, 129, 73

Scannapieco, E. & Oh, S. P. 2004, ApJ, 608, 62

Schlegel, D. J., Finkbeiner, D. P., & Davis, M. 1998, ApJ, 500, 525

Scott, J. E., Kriss, G. A., Lee, J. C., et al. 2004, ApJS, 152, 1

Shang, Z., Brotherton, M. S., Green, R. F., et al. 2005, ApJ, 619, 41

Silk, J. & Rees, M. J. 1998, A&A, 331, L1

Simon, L. E. & Hamann, F. 2010, MNRAS, 409, 269

Singh, K. P. & Westergaard, N. J. 1992, A&A, 264, 489

Somerville, R. S., Hopkins, P. F., Cox, T. J., Robertson, B. E., & Hernquist, L. 2008, MNRAS, 391, 481

Thom, C., Peek, J. E. G., Putman, M. E., et al. 2008, ApJ, 684, 364

Tombesi, F., Cappi, M., Reeves, J. N., et al. 2010, A&A, 521, A57

Treister, E., Urry, C. M., Schawinski, K., Cardamone, C. N., & Sanders, D. B. 2010, ApJ, 722, L238

Treister, E., Urry, C. M., & Virani, S. 2009, ApJ, 696, 110

Valenti, J. A., Lindler, D., Bowers, C., Busko, I., & Quijano, J. K. 2002, 2-D Algorithm for Removing Scattered Light from STIS Echelle Data, Tech. Rep. Instrument Science Report STIS 2002-001, STScI, Baltimore

Weymann, R. J., Williams, R. E., Peterson, B. M., & Turnshek, D. A. 1979, ApJ, 234, 33

Wu, C., Boggess, A., & Gull, T. R. 1980, ApJ, 242, 14

Yaqoob, T., McKernan, B., Kraemer, S. B., et al. 2003, ApJ, 582, 105

York, D. G., Ratcliff, S., Blades, J. C., et al. 1984, ApJ, 276, 92

Young, S. 2000, MNRAS, 312, 567

Young, S., Corbett, E. A., Giannuzzo, M. E., et al. 1999, MNRAS, 303, 227

Table 3. Emission Features in the COS Spectrum of Mrk 509

Feature	λ_0 (Å)	Flux (10^{-14} erg cm^{-2} s^{-1} Å^{-1})	v_{sys} (km s^{-1})	FWHM (km s^{-1})
Lyα	1215.670	9.1 ± 2.5	166 ± 31	300 ± 23
Lyα	1215.670	73.9 ± 2.5	−151 ± 15	1339 ± 33
Lyα	1215.670	410.0 ± 1.8	−235 ± 8	3039 ± 14
Lyα	1215.670	838.0 ± 1.8	−156 ± 7	9677 ± 26
N V	1238.821	22.1 ± 0.6	205 ± 22	2164 ± 45
N V	1242.804	11.1 ± 0.2	205 ± 22	2164 ± 45
Si II	1260.420	65.3 ± 1.0	−707 ± 36	5652 ± 66
O I+Si II	1303.57	31.5 ± 0.6	36 ± 33	3307 ± 90
C II	1335.205	8.0 ± 1.5	8 ± 67	2176 ± 424
Si IV	1393.755	85.0 ± 0.2	492 ± 9	5084 ± 36
Si IV	1402.770	42.5 ± 0.1	491 ± 9	5084 ± 36
C IV	1548.195	4.2 ± 1.4	−204 ± 39	300 ± 39
C IV	1550.770	2.1 ± 0.3	−204 ± 39	300 ± 39
C IV	1548.195	78.5 ± 0.5	−206 ± 7	1974 ± 15
C IV	1550.770	39.3 ± 0.5	−206 ± 7	1974 ± 15
C IV	1548.195	199.0 ± 1.9	−206 ± 7	4233 ± 15
C IV	1550.770	99.3 ± 1.9	−206 ± 7	4233 ± 15
C IV	1549.050	461.0 ± 1.1	158 ± 10	10299 ± 56
N IV]	1486.496	7.0 ± 0.1	−33 ± 61	2181 ± 108
Si II	1526.710	15.7 ± 1.3	2 ± 27	2181 ± 108
He II	1640.480	8.5 ± 0.3	−113 ± 39	1153 ± 83
He II	1640.480	55.4 ± 0.5	−199 ± 25	4065 ± 61
O III]	1663.445	66.0 ± 1.6	83 ± 19	3900 ± 69

Table 4. Emission Features in the STIS Spectrum of Mrk 509

Feature	λ_0 (Å)	Flux (10^{-14} erg cm^{-2} s^{-1} Å^{-1})	v_{sys} (km s^{-1})	FWHM (km s^{-1})
Lyα	1215.6700	6.8 ± 5.5	166 ± 575	300 ± 3
Lyα	1215.6700	102.0 ± 0.9	85 ± 15	1712 ± 66
Lyα	1215.6700	350.0 ± 2.9	−290 ± 4	3483 ± 25
Lyα	1215.6700	531.0 ± 4.4	−11 ± 19	10752 ± 56
N V	1238.8210	17.4 ± 0.3	371 ± 44	2089 ± 39
N V	1242.8040	8.7 ± 0.2	371 ± 44	2089 ± 39
Si II	1260.4200	36.1 ± 1.0	−921 ± 130	5928 ± 151
O I+Si II	1303.5700	21.8 ± 2.5	189 ± 62	3115 ± 94
C II	1335.2050	4.7 ± 2.4	106 ± 284	1555 ± 459
Si IV	1393.7550	54.9 ± 3.0	381 ± 194	4374 ± 97
Si IV	1402.7700	27.4 ± 1.5	382 ± 194	4374 ± 97
C IV	1548.1950	6.7 ± 1.8	−204 ± 151	300 ± 95
C IV	1550.7700	3.4 ± 0.9	−204 ± 151	300 ± 95
C IV	1548.1950	65.9 ± 3.6	−103 ± 7	2108 ± 30
C IV	1550.7700	33.0 ± 1.8	−103 ± 7	2108 ± 30
C IV	1548.1950	148.0 ± 2.0	−103 ± 7	4102 ± 93
C IV	1550.7700	74.1 ± 1.0	−103 ± 7	4102 ± 93
C IV	1549.0530	389.0 ± 1.5	−605 ± 10	9392 ± 156
N IV]	1486.4960	12.3 ± 0.6	262 ± 71	3795 ± 20
Si II	1526.7070	15.8 ± 1.4	−175 ± 86	3795 ± 20
He II	1640.4800	5.4 ± 0.8	38 ± 48	888 ± 135
He II	1640.4800	39.5 ± 3.1	−636 ± 67	4824 ± 104

Table 5. Emission Features in the 1999 FUSE Spectrum of Mrk 509

Feature	λ_0 (Å)	Flux (10^{-14} erg cm^{-2} s^{-1} Å^{-1})	v$_{\rm sys}$ (km s^{-1})	FWHM (km s^{-1})
C iii	977.0200	60.0 ± 4.7	−8 ± 25	4000 ± 172
N iii	989.7990	56.1 ± 1.8	−546 ± 51	8917 ± 217
Lyβ	1025.7220	0.6 ± 5.1	−812 ± 197	8917 ± 217
O vi	1031.9260	100.0 ± 3.2	−812 ± 197	8917 ± 217
O vi	1037.6170	50.1 ± 1.6	−812 ± 197	8917 ± 217
O vi	1031.9260	69.0 ± 3.1	193 ± 48	4182 ± 99
O vi	1037.6170	34.5 ± 1.6	193 ± 48	4182 ± 99
O vi	1031.9260	3.4 ± 0.6	−203 ± 33	300 ± 47
O vi	1037.6170	1.7 ± 0.3	−203 ± 33	300 ± 47

Table 6. Emission Features in the 2000 FUSE Spectrum of Mrk 509

Feature	λ_0 (Å)	Flux (10^{-14} erg cm^{-2} s^{-1} Å^{-1})	v$_{\rm sys}$ (km s^{-1})	FWHM (km s^{-1})
C iii	977.0200	26.8 ± 1.1	858 ± 665	9157 ± 860
C iii	977.0200	2.5 ± 0.1	137 ± 105	729 ± 277
N iii	989.7990	23.0 ± 1.6	−297 ± 245	7844 ± 187
Lyβ	1025.7220	0.1 ± 1.2	−566 ± 245	7844 ± 187
O vi	1031.9260	109.0 ± 5.0	−565 ± 245	7844 ± 187
O vi	1037.6170	54.3 ± 2.5	−564 ± 245	7844 ± 187
O vi	1031.9260	43.2 ± 4.0	199 ± 855	2585 ± 272
O vi	1037.6170	21.6 ± 2.0	199 ± 855	2585 ± 272
O vi	1031.9260	4.2 ± 1.0	−203 ± 129	300 ± 250
O vi	1037.6170	2.1 ± 0.5	−203 ± 129	300 ± 250

Table 9. Intrinsic Absorption Features in the COS Spectrum of Mrk 509

Ion	Component #	N (10^{12} cm^{-2})	v_{sys} (km s^{-1})	b (km s^{-1})	f_c
H I	1a	6.3 ± 0.7	−426 ± 5	13 ± 1	0.802 ± 0.087
H I	1	49.8 ± 4.9	−385 ± 7	30 ± 1	0.802 ± 0.087
H I	1b	2.2 ± 2.1	−361 ± 8	12 ± 2	0.802 ± 0.087
H I	2	349.7 ± 87.5	−316 ± 6	25 ± 1	0.965 ± 0.084
H I	2b	133.2 ± 66.1	−283 ± 5	26 ± 3	0.965 ± 0.084
H I	3	75.6 ± 9.2	−240 ± 7	32 ± 1	0.843 ± 0.126
H I	4a	262.0 ± 9.1	−59 ± 5	29 ± 1	0.953 ± 0.005
H I	4	134.9 ± 27.4	−8 ± 6	31 ± 1	0.984 ± 0.028
H I	5	217.3 ± 30.0	44 ± 8	42 ± 5	0.970 ± 0.024
H I	6a	34.6 ± 10.0	132 ± 7	33 ± 2	0.993 ± 0.024
H I	6	312.5 ± 35.6	125 ± 6	33 ± 2	0.993 ± 0.024
H I	6b	0.1 ± 1.0	166 ± 8	33 ± 2	0.993 ± 0.024
H I	7a	53.8 ± 12.8	185 ± 5	16 ± 3	0.861 ± 0.051
H I	7	123.9 ± 2.5	220 ± 5	32 ± 2	0.861 ± 0.051
N V	1	107.0 ± 9.5	−408 ± 5	10 ± 1	0.712 ± 0.026
N V	1b	17.5 ± 1.6	−375 ± 7	21 ± 3	0.678 ± 0.010
N V	2	149.0 ± 10.7	−321 ± 5	13 ± 1	0.950 ± 0.017
N V	2b	130.6 ± 11.3	−291 ± 6	19 ± 2	0.729 ± 0.025
N V	3	88.6 ± 8.1	−244 ± 5	16 ± 1	0.698 ± 0.045
N V	4a	93.6 ± 6.8	−59 ± 5	13 ± 1	0.945 ± 0.031
N V	4	323.6 ± 12.2	−19 ± 5	14 ± 1	1.000 ± 0.012
N V	5	38.3 ± 11.1	37 ± 5	13 ± 1	1.000 ± 0.250
N V	6a	20.6 ± 6.4	79 ± 7	41 ± 12	1.000 ± 0.023
N V	6	56.1 ± 4.0	121 ± 5	13 ± 1	1.000 ± 0.023
N V	6b	5.5 ± 1.8	147 ± 8	11 ± 3	1.000 ± 0.023
N V	7	21.0 ± 2.9	184 ± 6	16 ± 1	0.836 ± 0.094
N V	7a	23.5 ± 2.7	222 ± 6	16 ± 1	0.836 ± 0.094
Si IV	4	2.5 ± 0.2	−22 ± 6	10 ± 1	1.000 ± 0.146
C IV	1	31.2 ± 1.5	−406 ± 6	14 ± 1	0.892 ± 0.026
C IV	1b	16.3 ± 6.1	−365 ± 5	14 ± 1	0.935 ± 0.261
C IV	2	136.3 ± 41.7	−320 ± 6	13 ± 1	0.979 ± 0.035
C IV	2b	128.9 ± 41.4	−292 ± 7	22 ± 3	0.896 ± 0.030
C IV	3	44.7 ± 7.2	−245 ± 5	22 ± 2	0.987 ± 0.023
C IV	4a	66.3 ± 2.1	−60 ± 5	12 ± 1	0.961 ± 0.031
C IV	4	250.0 ± 11.0	−18 ± 5	16 ± 1	0.967 ± 0.007
C IV	5	36.2 ± 16.9	34 ± 5	19 ± 1	0.939 ± 0.109
C IV	6a	5.6 ± 2.3	88 ± 7	12 ± 2	0.986 ± 0.049
C IV	6	12.3 ± 6.4	122 ± 5	10 ± 1	0.986 ± 0.049
C IV	6b	17.6 ± 5.3	120 ± 8	24 ± 4	0.986 ± 0.049
C IV	7a	3.6 ± 1.1	171 ± 9	13 ± 2	0.892 ± 0.126
C IV	7	6.4 ± 0.8	232 ± 6	13 ± 2	0.892 ± 0.126

The scattered light component in this fit is 0.05 ± 0.01.

Table 10. Intrinsic Absorption Features in the STIS Spectrum of Mrk 509

Ion	Component #	N (10^{12} cm^{-2})	v_{sys} (km s^{-1})	b (km s^{-1})	f_c
H I	1a	11.6 ± 4.2	−428 ± 7	17 ± 2	0.561 ± 0.052
H I	1	63.9 ± 14.5	−380 ± 6	32 ± 5	0.561 ± 0.052
H I	1b	11.9 ± 9.2	−359 ± 6	14 ± 6	0.905 ± 0.052
H I	2	459.2 ± 276.4	−314 ± 7	24 ± 6	0.922 ± 0.019
H I	2b	86.8 ± 73.1	−283 ± 16	27 ± 12	0.850 ± 0.198
H I	3	87.5 ± 41.8	−237 ± 8	34 ± 4	0.861 ± 0.101
H I	4a	250.0 ± 98.3	−66 ± 6	30 ± 3	0.960 ± 0.010
H I	4	180.3 ± 38.0	−16 ± 9	18 ± 6	0.979 ± 0.026
H I	5	351.0 ± 75.2	37 ± 6	30 ± 7	0.958 ± 0.049
H I	6a	442.3 ± 188.9	137 ± 9	43 ± 2	0.998 ± 0.051
H I	6	401.4 ± 709.1	137 ± 26	43 ± 2	0.998 ± 0.051
H I	6b	6.8 ± 34.6	168 ± 152	43 ± 2	0.998 ± 0.051
H I	7a	75.5 ± 16.2	187 ± 134	19 ± 94	0.632 ± 0.277
H I	7	206.7 ± 28.6	220 ± 7	34 ± 4	0.632 ± 0.277
N V	1	95.5 ± 34.1	−408 ± 6	10 ± 1	0.562 ± 0.094
N V	1b	16.6 ± 29.8	−375 ± 6	21 ± 12	0.810 ± 0.104
N V	2	238.9 ± 56.2	−319 ± 7	12 ± 2	0.860 ± 0.072
N V	2b	91.7 ± 79.6	−291 ± 6	16 ± 5	0.809 ± 0.263
N V	3	94.0 ± 34.3	−246 ± 6	18 ± 3	0.759 ± 0.205
N V	4a	89.8 ± 21.6	−57 ± 6	14 ± 1	0.919 ± 0.133
N V	4	263.1 ± 23.3	−17 ± 6	17 ± 1	0.997 ± 0.074
N V	5	44.0 ± 25.9	34 ± 6	18 ± 2	0.999 ± 0.057
N V	6a	16.7 ± 7.1	79 ± 7	41 ± 6	0.997 ± 0.117
N V	6	46.8 ± 6.8	121 ± 6	12 ± 1	0.997 ± 0.117
N V	6b	5.2 ± 3.0	147 ± 9	11 ± 3	0.997 ± 0.117
N V	7a	25.1 ± 16.9	184 ± 8	16 ± 3	0.704 ± 0.231
N V	7	22.0 ± 14.8	222 ± 8	16 ± 3	0.704 ± 0.231
Si IV	4	3.5 ± 1.1	−18 ± 5	6 ± 1	0.946 ± 0.197
C IV	1	71.6 ± 19.6	−406 ± 6	12 ± 1	0.560 ± 0.276
C IV	1b	21.1 ± 5.7	−365 ± 5	27 ± 8	1.000 ± 0.110
C IV	2	144.2 ± 24.2	−320 ± 6	14 ± 1	0.983 ± 0.078
C IV	2b	137.9 ± 23.3	−292 ± 6	30 ± 5	0.893 ± 0.090
C IV	3	50.5 ± 27.8	−243 ± 7	25 ± 2	0.963 ± 0.031
C IV	4a	67.9 ± 8.5	−60 ± 6	13 ± 1	1.000 ± 0.069
C IV	4	233.7 ± 17.9	−18 ± 5	17 ± 1	0.960 ± 0.037
C IV	5	35.8 ± 45.6	36 ± 6	20 ± 1	0.916 ± 0.098
C IV	6a	0.1 ± 0.7	88 ± 68	12 ± 56	1.000 ± 0.045
C IV	6	16.1 ± 18.1	124 ± 1	13 ± 1	1.000 ± 0.045
C IV	6b	12.2 ± 7.1	120 ± 1	24 ± 1	1.000 ± 0.045
C IV	7a	1.1 ± 1.2	171 ± 6	6 ± 3	0.560 ± 0.276
C IV	7	6.1 ± 3.0	214 ± 2	6 ± 3	0.560 ± 0.276

The scattered light component in this fit is 0.01 ± 0.03.

Table 11. Intrinsic Absorption Features in the 1999 FUSE Spectrum of Mrk 509

Ion	Component	N	v_{sys}	b	f_c
	#	(10^{12} cm^{-2})	(km s^{-1})	(km s^{-1})	
H I	1a	24.4 ± 9.9	−433 ± 33	32 ± 14	0.991 ± 0.004
H I	1	363.3 ± 9.1	−411 ± 7	31 ± 3	0.991 ± 0.004
H I	1b	0.3 ± 2.8	−383 ± 134	15 ± 99	0.991 ± 0.004
H I	2	549.4 ± 61.9	−323 ± 6	19 ± 3	0.978 ± 0.036
H I	2b	58.1 ± 55.3	−292 ± 5	12 ± 6	0.826 ± 0.246
H I	3	681.5 ± 104.9	−258 ± 8	31 ± 3	0.869 ± 0.037
H I	4a	1924.1 ± 154.4	−35 ± 8	43 ± 2	0.939 ± 0.029
H I	4	2594.9 ± 1146.8	−29 ± 7	23 ± 3	0.902 ± 0.088
H I	5	359.5 ± 45.2	27 ± 9	32 ± 9	0.999 ± 0.116
H I	6a	114.3 ± 92.8	75 ± 14	32 ± 1	0.902 ± 0.020
H I	6	520.3 ± 93.7	115 ± 6	32 ± 1	0.902 ± 0.020
H I	6b	168.4 ± 1.7	129 ± 13	32 ± 1	0.902 ± 0.020
H I	7a	154.4 ± 73.9	174 ± 8	19 ± 4	0.905 ± 0.154
H I	7	227.8 ± 118.6	211 ± 8	24 ± 7	0.969 ± 0.098
O VI	1a	0.7 ± 5.5	−427 ± 33	9 ± 11	0.697 ± 0.072
O VI	1	215.0 ± 47.2	−388 ± 8	22 ± 2	0.697 ± 0.072
O VI	1b	154.9 ± 39.0	−360 ± 5	22 ± 2	0.697 ± 0.072
O VI	2	566.2 ± 118.0	−318 ± 5	19 ± 3	0.926 ± 0.076
O VI	2b	1248.1 ± 395.5	−290 ± 5	17 ± 2	0.919 ± 0.037
O VI	3	675.2 ± 157.1	−247 ± 5	28 ± 3	0.814 ± 0.048
O VI	4a	804.5 ± 387.2	−65 ± 5	15 ± 2	0.714 ± 0.049
O VI	4	8797.0 ± 4120.3	−9 ± 5	28 ± 3	1.000 ± 0.008
O VI	5	683.5 ± 429.3	47 ± 5	24 ± 22	1.000 ± 0.032
O VI	6a	518.8 ± 398.5	87 ± 5	15 ± 21	0.949 ± 0.160
O VI	6	3436.1 ± 6985.0	120 ± 6	12 ± 7	1.000 ± 0.014
O VI	6b	104.5 ± 234.6	146 ± 5	12 ± 7	1.000 ± 0.014
O VI	7a	660.2 ± 176.7	179 ± 41	22 ± 78	0.834 ± 0.191
O VI	7	667.4 ± 1105.3	213 ± 17	26 ± 8	1.000 ± 0.023

The scattered light component in this fit is 0.04 ± 0.02.

Table 12. Intrinsic Absorption Features in the 2000 FUSE Spectrum of Mrk 509

Ion	Component	N	v_{sys}	b	f_c
	#	(10^{12} cm^{-2})	(km s^{-1})	(km s^{-1})	
H I	1a	31.1 ± 41.1	−425 ± 8	29 ± 25	1.000 ± 0.071
H I	1	302.5 ± 41.9	−402 ± 5	28 ± 2	1.000 ± 0.071
H I	1b	0.3 ± 2.8	−371 ± 118	15 ± 19	1.000 ± 0.071
H I	2	563.0 ± 167.1	−318 ± 5	24 ± 5	0.970 ± 0.078
H I	2b	75.9 ± 69.2	−281 ± 8	16 ± 7	0.890 ± 0.072
H I	3	824.6 ± 51.5	−250 ± 5	28 ± 1	0.793 ± 0.061
H I	4a	3493.7 ± 12430.4	−35 ± 54	34 ± 21	0.904 ± 0.093
H I	4	2506.3 ± 9025.3	−4 ± 48	27 ± 66	0.793 ± 0.159
H I	5	327.8 ± 37.1	47 ± 53	25 ± 20	1.000 ± 0.027
H I	6a	175.9 ± 275.9	89 ± 107	31 ± 30	1.000 ± 0.027
H I	6	655.7 ± 1019.0	123 ± 12	31 ± 30	1.000 ± 0.027
H I	6b	138.0 ± 358.2	166 ± 138	31 ± 30	1.000 ± 0.027
H I	7a	365.8 ± 282.3	185 ± 6	17 ± 44	0.565 ± 0.394
H I	7	243.4 ± 81.4	217 ± 26	25 ± 162	1.000 ± 0.027
O VI	1a	16.5 ± 17.6	−427 ± 5	9 ± 5	0.697 ± 0.271
O VI	1	154.9 ± 113.5	−396 ± 6	17 ± 7	0.697 ± 0.271
O VI	1b	210.5 ± 123.3	−363 ± 15	17 ± 7	0.697 ± 0.271
O VI	2	968.3 ± 187.2	−312 ± 5	18 ± 4	0.926 ± 0.025
O VI	2b	125.6 ± 68.6	−281 ± 7	15 ± 6	0.919 ± 0.103
O VI	3	917.3 ± 181.2	−256 ± 5	39 ± 2	0.814 ± 0.065
O VI	4a	640.6 ± 68.3	−56 ± 5	23 ± 2	0.924 ± 0.008
O VI	4	1293.2 ± 735.3	−9 ± 6	20 ± 1	1.000 ± 0.015
O VI	5	569.2 ± 275.9	36 ± 10	20 ± 1	1.000 ± 0.052
O VI	6a	324.8 ± 179.7	64 ± 13	20 ± 1	0.949 ± 0.082
O VI	6	565.4 ± 46.2	104 ± 5	20 ± 1	1.000 ± 0.027
O VI	6b	362.4 ± 59.3	137 ± 6	20 ± 1	1.000 ± 0.027
O VI	7a	403.8 ± 187.2	185 ± 6	20 ± 1	0.834 ± 0.160
O VI	7	640.3 ± 217.3	213 ± 5	25 ± 1	1.000 ± 0.019

The scattered light component in this fit is 0.05 ± 0.01.